

1 **The role of surface potential vorticity in the vertical structure of mesoscale**
2 **eddies**

3 Wenda Zhang^a, Stephen M. Griffies^{a,b}, Robert W. Hallberg^{a,b}, Yi-Hung Kuo^a, Christopher L.
4 P. Wolfe^c

5 ^a *Program in Atmospheric and Oceanic Sciences, Princeton University, Princeton, NJ, USA*

6 ^b *NOAA/Geophysical Fluid Dynamics Laboratory, Princeton, NJ, USA*

7 ^c *School of Marine and Atmospheric Sciences, Stony Brook University, Stony Brook, NY, USA*

8 *Corresponding author: Wenda Zhang, wenda.zhang@princeton.edu*

9 ABSTRACT: The vertical structure of ocean eddies is generally surface-intensified, commonly
10 attributed to the dominant baroclinic modes arising from boundary conditions (BCs). Conventional
11 BC consideration mostly focuses on either flat- or rough-bottom conditions. The impact of surface
12 buoyancy anomaly—often represented by surface potential vorticity (PV) anomaly—has not been
13 fully explored. Here, we study the role of the surface PV in setting the vertical distribution of eddy
14 kinetic energy (EKE) in an idealized adiabatic ocean model. The simulated EKE profile in the extra-
15 tropical ocean tends to peak at the surface and have an e -folding depth typically smaller than half
16 of the ocean depth. This vertical structure can be reasonably represented by a single surface quasi-
17 geostrophic (SQG) mode at the energy-containing scale resulting from surface-trapped baroclinic
18 instability and inverse energy cascades. The surface meridional PV gradient—key to oceanic
19 baroclinic instability—induces surface-trapped unstable modes that decay faster with depth for
20 smaller horizontal scales. Subsequently, through an inverse energy cascade from scales close
21 to or smaller than the deformation radius to the energy-containing scale, the vertical structure
22 grows deeper while remaining surface-trapped. These results indicate that the vertical EKE
23 distribution depends on the horizontal scale since smaller eddies tend to be shallower. Guided
24 by this interpretation, an SQG-based scale-aware parameterization of the EKE profile is proposed
25 here. Preliminary offline diagnosis of a high-resolution simulation shows the proposed scheme
26 successfully reproducing the dependence of the vertical structure of EKE on the horizontal grid
27 resolution.

28 **1. Introduction**

29 Ocean mesoscale eddies including horizontal scales of tens to hundreds of kilometers account
30 for a majority of oceanic kinetic energy (e.g., Ferrari and Wunsch 2009; Storer et al. 2022). These
31 eddies are important to the transport and mixing of momentum, heat, salt, carbon, as well as other
32 biogeochemical tracers, and impact the large-scale circulation and climate (Wolfe and Cessi 2010;
33 Marshall and Speer 2012; Griffies et al. 2015; Gnanadesikan et al. 2015). These eddies are yet to be
34 fully-resolved in climate models due to their relatively small size and as a result, their effects must
35 be parameterized. Observational and modeling studies have shown that the strength of mesoscale
36 eddies tend to peak at the surface and decay with depth (Wunsch 1997; de La Lama et al. 2016),
37 with the exception for certain mode-water or topographically trapped eddies that intensify in the
38 interior or near the bottom (Zhang et al. 2017; Radko 2023). Parameterizations that properly
39 account for the surface-intensified vertical structure are crucial for simulations of large-scale ocean
40 circulations and density structures (Danabasoglu and Marshall 2007; Eden et al. 2009). This effort
41 requires a better understanding and representation of the eddy vertical structure, which is the topic
42 of this paper.

43 The vertical structure of eddy motions is often represented using vertical normal modes (Wunsch
44 1997; Wortham and Wunsch 2014; de La Lama et al. 2016). Traditionally, these modes—including
45 the barotropic and baroclinic modes—are solutions to an eigenvalue problem with flat-bottom and
46 rigid-lid boundary conditions (Gill 1982; Vallis 2017). The surface-intensified structure of ocean
47 eddies is then decomposed as a linear combination of these eigenmodes in the vertical.

48 Notably, the barotropic and first baroclinic modes together can capture the bulk of mid-latitude
49 eddy structure and variability (Wunsch 1997; Zhang et al. 2013). That these two modes are
50 dominant is consistent with geostrophic turbulence theory, which reveals that eddies emerging
51 from baroclinic instability tend to transfer energy from higher baroclinic modes to the lower modes
52 and then to the barotropic mode at scales comparable to the deformation radius (Salmon 1980;
53 Smith and Vallis 2001). Due to surface-intensified stratification and bottom friction, ocean eddies
54 are usually not fully barotropized and the first-baroclinic contribution remains considerable (Fu and
55 Flierl 1980; Smith and Vallis 2001). Although the barotropic and first baroclinic modes are useful
56 for diagnosing the vertical structure of eddies, they are inefficient for quantitative predictions since
57 their relative contribution to eddy energy varies substantially in space and time (Wunsch 1997).

58 Vertical mode structures can change significantly in the presence of bottom topography (Hallberg
59 1997; Lacasce 2017), leading to recent studies promoting a different set of baroclinic modes subject
60 to zero horizontal velocity at the bottom due to rough bathymetry (Lacasce 2017). The inclusion
61 of the *rough bottom* tends to decouple the bottom pressure from the interior, yielding modified
62 baroclinic structures that are more surface-intensified (Rhines 1970; Hallberg 1997; Samelson
63 1992; Tailleux and McWilliams 2001). The first baroclinic mode derived under such rough-bottom
64 setup is more consistent with observations than the traditional mode (de La Lama et al. 2016;
65 Ni et al. 2023), and has recently been used for diagnoses and parameterizations of the vertical
66 structure of eddy velocity and mixing (Adcroft et al. 2019; Groeskamp et al. 2020; Stanley et al.
67 2020; Holmes et al. 2022).

68 Still, these rough-bottom modes assume a zero buoyancy anomaly at the ocean surface, whereas
69 ocean eddies exhibit strong surface temperature and salinity anomalies (Lapeyre 2009; Hausmann
70 and Czaja 2012; Frenger et al. 2015). Theoretical studies indicate that a complete vertical-mode
71 analysis should include surface buoyancy anomalies that give rise to surface-trapped responses that
72 decay quasi-exponentially from the surface (Smith and Vanneste 2013; Yassin and Griffies 2022a).
73 The surface-trapped mode is governed by the surface quasi-geostrophic (SQG) dynamics in the
74 presence of a surface horizontal buoyancy gradient (Blumen 1978; Held et al. 1995; Lapeyre and
75 Klein 2006; Lapeyre 2017). Previous studies noted that the SQG mode can capture the surface
76 intensification of the observed eddies better than the traditional baroclinic structures, pointing to
77 surface buoyancy anomalies being key to establishing the vertical distribution of ocean eddies
78 (Lapeyre and Klein 2006; Lapeyre 2009).

79 The SQG framework has been adapted to infer the eddy properties in the vertical from surface
80 observations and hydrography in the midlatitude ocean in both modeling (Lapeyre and Klein 2006;
81 Isern-Fontanet et al. 2008; Wang et al. 2013; Ponte and Klein 2013; Liu et al. 2014; Qiu et al. 2016;
82 Fresnay et al. 2018; Qiu et al. 2020; Miracca-Lage et al. 2022) and observational studies (LaCasce
83 and Mahadevan 2006; Liu et al. 2017). Such inference, however, depends on the spectra of the
84 surface eddy energy or buoyancy—seemingly limiting the application of the SQG framework
85 to the parameterization of eddies for ocean models in which mesoscale features are not fully
86 resolved. Here, we argue that the energy-containing scale comparable to the deformation radius is
87 sufficient to determine the dominant SQG mode and its vertical distribution. Assuming the energy-

88 containing scale is given and using this in lieu of the full surface spectra, an SQG-based, scale-aware
89 parameterization for ocean eddy is proposed in this study. Focusing on the dependence of vertical
90 structure on horizontal scales, offline analyses with output from an idealized adiabatic ocean model
91 demonstrate that the proposed scheme reproduces the desired distributions of unresolved eddies
92 by models with different horizontal resolutions. The only remaining step for a completely closed
93 parameterization is the determination of the horizontal energy-containing scale.

94 Why does the SQG mode at the energy-containing scale play such an important role in the
95 vertical eddy structure? The geostrophic turbulence theory provides a potential explanation.
96 Surface buoyancy anomalies are often represented as surface-confined potential vorticity (PV)
97 anomalies (Bretherton 1966). The horizontal PV gradient—important for baroclinic instability—
98 tends to be substantial at the ocean surface, yielding surface-trapped unstable modes (Smith 2007;
99 Fox-Kemper et al. 2008a; Tulloch et al. 2011; Callies et al. 2016; Feng et al. 2021, 2022). Surface-
100 trapped instabilities can efficiently energize submesoscale processes, which in turn energize the
101 mesoscale eddies via an inverse energy cascade (Roulet et al. 2012; Callies et al. 2016; Capet
102 et al. 2016; Schubert et al. 2020; Khatri et al. 2021). That is, a surface PV (buoyancy) gradient can
103 indirectly supply energy to mesoscale eddies via the surface-trapped submesoscale instabilities.

104 This hypothesized link between baroclinic instability and the vertical structure of mesoscale
105 eddies are also investigated here in an idealized adiabatic ocean model. We examine the eddy
106 kinetic energy (EKE) in circulation regimes analogous to those in the Atlantic Ocean. The
107 simulated EKE exhibits i) a surface-intensified profile consistent with the SQG mode at the energy-
108 containing scale; and ii) a dependence of vertical distribution on the horizontal eddy scale—smaller
109 eddies tend to have shallower structures. Although this model does not have surface buoyancy
110 forcing and a mixed layer, the isopycnal outcropping due to wind forcing gives rise to a strong
111 surface PV gradient, which generates surface-trapped unstable modes. These unstable modes
112 supply energy to the energy-containing eddy through the inverse cascade and in turn determines
113 the EKE profile.

114 This manuscript is organized as follows. Section 2 covers equations of the baroclinic and
115 surface-trapped modes for theoretical background. The numerical model configuration and WKB
116 solutions for the SQG mode are given in Section 3. In Section 4, we reveal the key role of
117 SQG modes in setting the vertical structure of EKE, which can be determined by the horizontal

118 energy-containing scale. In Section 5, we argue that the dominance of the SQG mode arises from
 119 baroclinic instability and the corresponding inverse energy cascade, which are surface-trapped due
 120 to the upper-ocean density structures. Based on these understandings, in Section 6 we propose
 121 a SQG-based parameterization for the subgrid EKE profile that depends on the model horizontal
 122 resolution. The results are summarized, and their implications for understanding the eddy vertical
 123 structure are discussed in Section 7.

124 2. Theoretical Background

125 In this section, we recap elements from quasi-geostrophic (QG) theory, focusing on (i) the
 126 vertical structure of baroclinic modes; and (ii) modifications to take into account the surface
 127 buoyancy anomaly.

128 *a. Baroclinic Modes*

129 The vertical structure of ocean eddies is commonly represented using the vertical normal modes
 130 of the linearized QG equations for a quiescent ocean state (e.g., chapter 6 of Vallis 2017),

$$\frac{\partial}{\partial t} \left[\nabla^2 \psi + \frac{\partial}{\partial z} \left(\frac{f^2}{N^2} \frac{\partial \psi}{\partial z} \right) \right] + \beta \frac{\partial \psi}{\partial x} = 0, \quad (1)$$

131 where $\psi(x, y, z, t)$ is the streamfunction perturbation, f the Coriolis parameter, β the meridional
 132 derivative of f , and $N^2 = \partial B / \partial z$ the squared buoyancy frequency defined via the large-scale
 133 buoyancy B . Note that ψ and $\partial \psi / \partial z$ are proportional to the pressure and buoyancy anomalies,
 134 respectively.

135 Substituting the wave-like ansatz

$$\psi = \hat{\psi}_0 \Phi(z) \exp[i(k_x x + k_y y - \omega t)] \quad (2)$$

136 into equation (1) yields an eigenvalue problem for the vertical structure function Φ

$$\frac{d}{dz} \left(\frac{f^2}{N^2} \frac{d\Phi}{dz} \right) = -\lambda^2 \Phi. \quad (3)$$

137 Here, $\hat{\psi}_0$ is proportional to the 2D Fourier transform of ψ at the surface, k_x and k_y the zonal
 138 and meridional wavenumber, respectively, ω the frequency, and λ^2 the reciprocal of squared
 139 deformation radius.

140 Solving equation (3) requires surface and bottom boundary conditions (BCs). It is common to
 141 assume the flat-bottom and rigid-lid conditions in which the buoyancy vanishes

$$\frac{d\Phi}{dz} = 0 \text{ at } z = 0, -H. \quad (4)$$

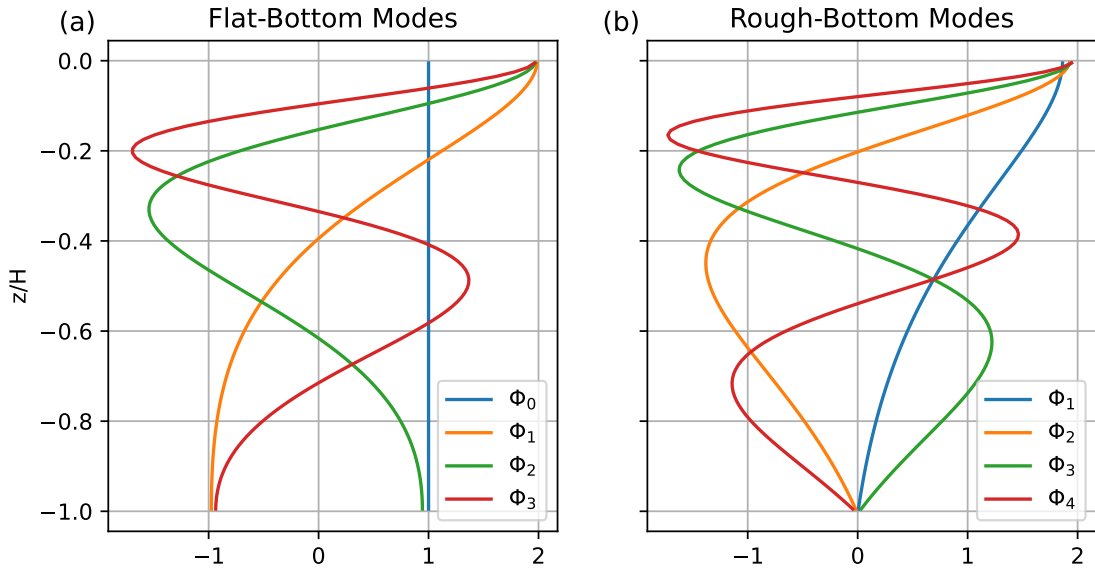
142 Equations (3) and (4) constitute a Sturm-Liouville problem for Φ , admitting a set of orthogonal
 143 normal modes $\{\Phi_m\}$ with the corresponding eigenvalues $\{\lambda_m^2\}$. Here the index $m \geq 0$ counts the
 144 number of zeros of $\Phi_m(z)$ in the interior. The solution with $m = 0$ denotes the barotropic mode,
 145 and the infinity of $m \geq 1$ solutions are the baroclinic modes. The first few modes are shown in
 146 Fig. 1a as computed with an exponential stratification profile whose e-folding scale is a third of
 147 water depth. General solutions of the eddy satisfying equation (1) and the same BCs (4) can be
 148 uniquely represented as a linear combination of these modes.

149 An alternative structural consideration includes the bottom topography (Rhines 1970; Hallberg
 150 1997) with which the horizontal velocity vanishes at the bottom, yielding

$$\frac{d\Phi}{dz} = 0 \text{ at } z = 0 \text{ and } \Phi = 0 \text{ at } z = -H. \quad (5)$$

151 That is, the bottom BC is now imposed on the pressure anomaly. These alternative BCs result
 152 in a different set of normal modes shown in Fig. 1b, referred to as the *rough-bottom* modes or
 153 “surface modes” in Lacasce (2017) since the bottom horizontal flow is at rest. Notably, there is not
 154 a depth-independent barotropic mode among these—an important distinction from the flat-bottom
 155 modes in Fig.1a. The barotropic mode is replaced by bottom-trapped topographic waves (e.g.,
 156 Rhines 1970; Lacasce 2017; Yassin and Griffies 2022a) not illustrated here. The lowest rough-
 157 bottom mode ($m = 1$; blue line in Fig.1b)—because it does not change sign in the interior—is
 158 often referred as the equivalent barotropic (EBT) mode (Killworth 1992; Hallberg 1997; Adcroft
 159 et al. 2019). The EBT mode has been adapted for the parameterization of the vertical distribution
 160 of mesoscale eddy diffusivity, e.g., in the 0.5° version of the GFDL ocean climate model OM4.0
 161 (Adcroft et al. 2019).

162 A notable feature of the two Sturm-Liouville problems considered thus far is that the horizontal
 163 wavenumbers do not appear in them, except for the bottom topographic waves. Therefore, the
 164 vertical structure of the normal modes do not depend on the horizontal scales. This can be
 165 attributed to the surface boundary conditions not including buoyancy anomalies (i.e., $d\Phi/dz = 0$
 166 at $z = 0$)—an assumption shared by both of the flat- and rough-bottom setups that is inconsistent
 167 with the SST observations exhibiting warm- and cold-core eddies (Lapeyre 2009; Hausmann and
 168 Czaja 2012; Frenger et al. 2015).



169 FIG. 1. The first four vertical normal modes solved from the eigenvalue problem (3) with (a) flat bottom and
 170 rigid lid boundaries, and (b) rough bottom and rigid lid boundaries. The stratification decays exponentially with
 171 depth following an e-folding scale of a third of the water depth in both cases. Each profile of Φ_m is normalized so
 172 that $\int_{-H}^0 \Phi_m^2 dz/H = 1$. Blue, orange, green, and red lines indicate the first, second, third, and fourth modes. The
 173 first mode, Φ_0 in (a) is depth independent and called the barotropic mode, while the other modes are baroclinic
 174 (BC) modes. The Φ_0 mode in (b) is represented by bottom-trapped topographic waves, which are not plotted
 175 here. The first mode, Φ_1 , in (b) is often called the equivalent barotropic (EBT) mode.

176 *b. Surface-Trapped Modes*

177 To incorporate surface buoyancy anomalies, a surface-aware formulation is proposed to include
 178 the horizontal buoyancy gradient at the surface (and bottom), as briefly outlined here following
 179 Smith and Vanneste (2013) as well as Yassin and Griffies (2022a).

180 In this modified approach, the eigenvalue problem consists of the same differential equation (3)
 181 but with a set of more general BCs

$$\begin{aligned} \frac{f^2}{N^2 H} \frac{d\Phi}{dz} &= \alpha(0)(k^2 + \lambda^2)\Phi, \text{ at } z = 0, \\ \frac{f^2}{N^2 H} \frac{d\Phi}{dz} &= -\alpha(-H)(k^2 + \lambda^2)\Phi, \text{ at } z = -H, \end{aligned} \quad (6)$$

182 with a non-dimensional function

$$\alpha(z) \equiv \frac{f}{N^2 \beta k_x} \left(k_x \frac{\partial B}{\partial y} - k_y \frac{\partial B}{\partial x} \right), \quad (7)$$

183 $k = (k_x^2 + k_y^2)^{1/2}$, and B the large-scale buoyancy. The resulting system differs from the standard
 184 Sturm-Liouville problem in that the wavenumbers k , k_x , k_y and eigenvalue λ^2 are now part of
 185 the BCs. Following Smith and Vanneste (2013), the most relevant case for our discussion here is
 186 the limit where $\alpha(-H) \rightarrow 0$ (i.e., the buoyancy anomaly vanishes at the bottom) and $\alpha(0) \rightarrow \infty$
 187 (strong horizontal buoyancy gradient and/or weak vertical stratification at the surface). The full set
 188 of normal modes in this case consists of a surface-trapped mode $\Phi_s(z; k)$ satisfying

$$\begin{aligned} \frac{d}{dz} \left(\frac{f^2}{N^2} \frac{d\Phi_s}{dz} \right) &= k^2 \Phi_s, \\ \Phi_s|_{z=0} &= 1, \\ \frac{d\Phi_s}{dz} \Big|_{z=-H} &= 0, \end{aligned} \quad (8)$$

189 and the interior modes $\Phi_m(z)$ (for integral index $m \geq 1$)

$$\begin{aligned} \frac{d}{dz} \left(\frac{f^2}{N^2} \frac{d\Phi_m}{dz} \right) &= -\lambda_m^2 \Phi_m, \\ \Phi_m|_{z=0} &= 0, \\ \frac{d\Phi_m}{dz} \Big|_{z=-H} &= 0. \end{aligned} \tag{9}$$

190 A few examples of these modes are illustrated in Fig. 2. Together, the admissible Φ_s and Φ_m
191 form an orthogonal basis, which is different from the decomposition of eddy flow into surface and
192 interior solutions by Lapeyre and Klein (2006). See Appendix A for detailed comparison.

193 Note the similarity between equation (9) and the earlier rough-bottom setup (the surface and
194 bottom BCs are switched here). Especially, the vertical structure of the interior modes does not
195 depend on horizontal scales (see Fig. 2b).

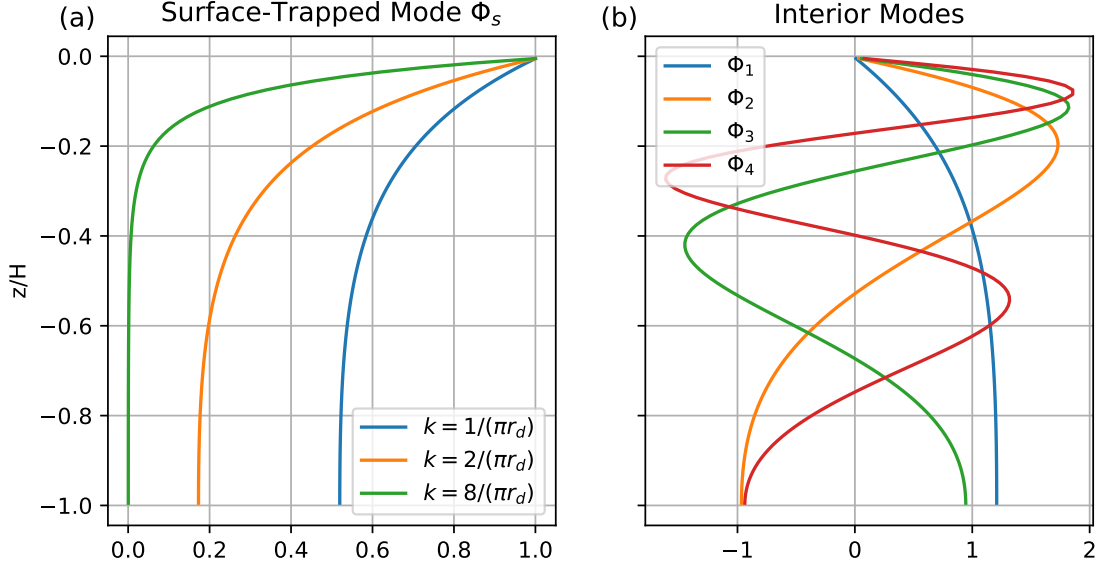
196 In contrast, equation (8) explicitly includes the horizontal wavenumber, yielding an outstanding
197 feature of the surface-trapped mode: Larger eddies (with smaller horizontal wavenumber k) tend
198 to be associated with deeper modes whose vertical response decays slower with depth; see Fig. 2a.
199 Because Φ_s has a zero interior PV anomaly and is driven by a surface buoyancy anomaly—
200 consistent with the surface QG (SQG) dynamics (Blumen 1978; Held et al. 1995)—it is also
201 referred to as the “SQG mode.” The SQG mode is relevant to the oceanic cases where horizontal
202 buoyancy gradient intensifies near the surface (Smith 2007; Capet et al. 2016), and is central for
203 this paper.

204 Both of the surface-trapped and interior modes described above assume a flat-bottom condition,
205 i.e., vanishing buoyancy anomaly; recall the bottom BCs in equations (8) and (9). These are the
206 limiting cases of equation (6) through which more complicated topographic effects can be included
207 (Lacasce 2017; Yassin and Griffies 2022a) and will be explored in future work.

214 3. Methods

215 *a. Model Configuration*

216 The numerical model used in this study is an idealized configuration of the Modular Ocean
217 Model version 6 (MOM6). This configuration is named “Neverworld2” by Marques et al. (2022)
218 and has been used to study mesoscale eddy parameterizations (e.g., Loose et al. 2022; Yankovsky



208 FIG. 2. Vertical profiles of the (a) surface-trapped mode and (b) interior modes, determined by solving equations
 209 (8), and (9), respectively. The stratification profile is an exponential function of z , as in Fig. 1. The surface mode
 210 is calculated for three different horizontal wavenumbers, $1/(\pi r_d)$, $2/(\pi r_d)$, and $8/(\pi r_d)$, where r_d is the Rossby
 211 deformation radius of the first flat-bottom baroclinic mode (orange line in Fig. 1a). Each surface-trapped mode
 212 profile is normalized by its surface value. The lines in panel (b) indicate the first four interior modes, each of
 213 which is normalized in the same way as the modes in Fig. 1.

219 et al. 2022). The model domain is a single basin with two hemispheres using spherical coordinates.
 220 The domain extends from -70°S to 70°N in the meridional direction, $0-60^\circ$ in the zonal direction,
 221 and has a maximum depth of 4000 m. The domain is bounded by a 200-m continental shelf along
 222 all side boundaries, except for a zonally reentrant channel located at 60°S to 40°S , mimicking the
 223 Southern Ocean. A ridge topography orienting meridionally spans the entire meridional extent of
 224 the domain. The ridge has a width of 40° and maximum height of 2000 m. There is a semi-circular
 225 ridge with radius of 10° spanning 0° to 10° longitude and 60°S to 40°S latitude that mimics the
 226 Scotia Arc across the Drake Passage.

227 The hydrostatic primitive equations are discretized in the vertical using isopycnal coordinates,
 228 with a total of 15 isopycnal layers with finer spacing near the surface in the initial setup. The
 229 horizontal grid spacing is $1/32^\circ$. The model is driven solely via mechanical forcing from a zonally
 230 uniform zonal wind stress that varies meridionally and is fixed in time. There is no surface buoyancy

231 forcing, no diabatic mixing, nor is there a mixed layer parameterization (i.e., it is a wind-driven
 232 stacked shallow water model). Dissipation arises from a background kinematic vertical viscosity
 233 ($A_v = 1.0 \times 10^{-4} \text{ m}^2 \text{ s}^{-1}$), a dimensionless bottom drag ($C_d = 0.003$), and the horizontal friction
 234 given by a biharmonic Smagorinsky viscosity (Griffies and Hallberg 2000). More details about the
 235 model setup and spinup are given in Marques et al. (2022).

242 Fig. 3a shows a snapshot of the surface specific kinetic energy (KE). The black lines correspond
 243 to the 500-day mean sea surface height (SSH) contours, representing the streamlines of surface
 244 geostrophic currents outside the tropics. The circulation pattern is a caricature of the Atlantic
 245 Ocean, with subtropical gyres and western boundary currents in both hemispheres. In the northern
 246 hemisphere, there is a subpolar gyre, while in the southern hemisphere, a circumpolar current
 247 prevails in the reentrant channel. The KE illustrates the prevalence of mesoscale eddies throughout
 248 the domain. The Rossby deformation radius is resolved over most regions of the model, with the
 249 exception being the continental shelf and very high latitudes near the boundaries (Yankovsky et al.
 250 2022).

251 *b. Solution for the SQG Mode*

252 The SQG mode, Φ_s , described by equations (8), is diagnosed in the stacked shallow water model
 253 introduced above. In this model, the dynamical impact of surface buoyancy is represented by the
 254 surface-layer PV, as described by the layered QG dynamics detailed in Appendix B.

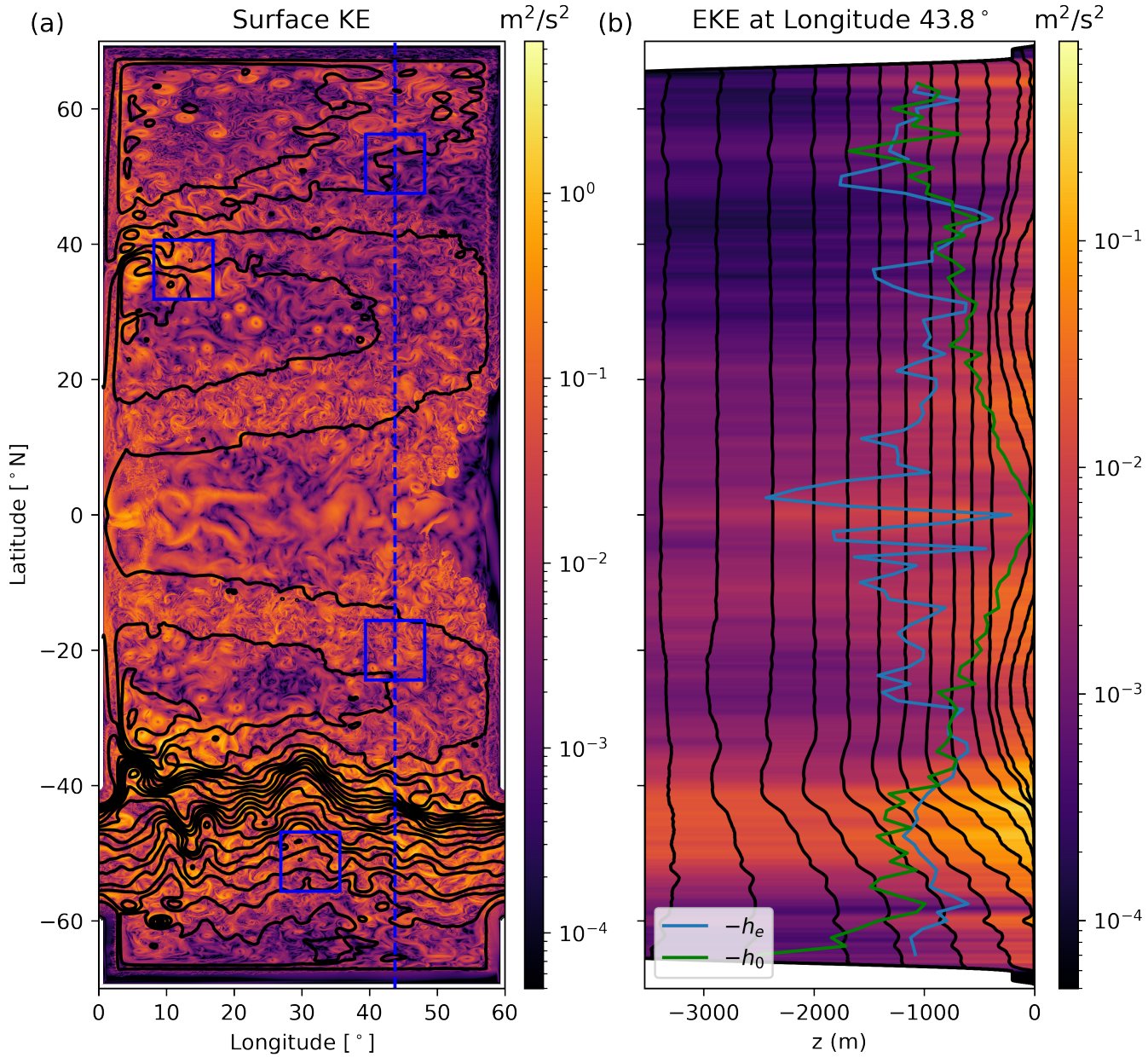
255 The SQG mode can be determined numerically for realistic stratification profiles. We can also
 256 derive an analytical solution using the WKB approximation. To get a simple analytical form, we
 257 assume $\Phi_s \rightarrow 0$ if $z \rightarrow -\infty$. For each horizontal wavenumber k , the WKB solution, Φ_s^{WKB} , is given
 258 to the first order by,

$$\Phi_s^{\text{WKB}} = e^{kz_s}, \quad (10)$$

259 where

$$z_s = - \int_z^0 \frac{N}{|f|} dz, \quad (11)$$

260 is the stretched vertical coordinate with $z < 0$ and $z_s < 0$ in the ocean interior.



236 FIG. 3. (a) Snapshot of horizontal kinetic energy at the surface. Black lines are contours of the 500-day mean
 237 sea surface height (SSH). The four blue boxes indicate the $8.7^\circ \times 8.7^\circ$ regions where the vertical structure of
 238 eddies is analyzed in later figures. Panel (b) shows a meridional section of the eddy kinetic energy per unit mass
 239 along the longitude shown by the blue dashed line in panel (a). Black lines show all the isopycnals in the model.
 240 Blue lines indicate the e-folding depth, h_e , of the rms eddy velocity (square root of EKE). Green line is the
 241 deformation depth, h_0 , of the energy-containing scale, introduced in section 4b.

261 The Fourier transform of the streamfunction field associated with the SQG mode, $\hat{\psi}_s$, is

$$\hat{\psi}_s^{\text{WKB}} = \hat{\psi}_0 e^{kz_s}, \quad (12)$$

262 where $\hat{\psi}_0$ is the same as that in equation (2), which is the Fourier transform of the streamfunction
263 at the surface.

264 Equation (10) reveals important characteristics of the SQG mode, namely, its exponential decay
265 with z_s and its dependence on the horizontal scale of eddies. Smaller eddies with larger wavenum-
266 ber, k , decay faster with depth than larger eddies with smaller wavenumber. The scale dependence
267 of the SQG mode provides valuable insights for parameterizing the vertical structure of eddies,
268 as we discuss in Section 6.

269 Note that equation (10) differs from the widely used “eSQG” method in ocean studies (Lapeyre
270 and Klein 2006). The eSQG method assumes a constant N with depth, determined empirically
271 to account for the impact of an internal PV gradient (Lapeyre and Klein 2006). In contrast, our
272 formula accounts for the vertical variation of N within the stretched vertical coordinate z_s , allowing
273 for a more accurate representation of the SQG mode itself. See also Yassin and Griffies (2022b)
274 for more on SQG theory with vertically varying stratification.

275 4. Vertical Structure of EKE

276 We analyze the vertical structure of EKE, defined as

$$\text{EKE} = \frac{1}{2} \left(\overline{u'^2} + \overline{v'^2} \right), \quad (13)$$

277 where $\bar{\cdot}$ indicates a 500-day mean, and \cdot' is the anomaly from the mean and is saved in snapshots
278 in 5-day intervals. Fig. 3b shows the EKE along a meridional section indicated by the blue dashed
279 line in Fig. 3a. The EKE tends to be surface-intensified. It maximizes at the surface and rapidly
280 decays with depth in the gyre and low latitudes, while it remains significant in the deep ocean
281 in the circumpolar current. To examine the detailed vertical structure, we select four distinct
282 dynamical regions, highlighted by the four blue boxes in Fig. 3a, that are located in the circumpolar
283 current, subtropical gyre, western boundary current extension, and subpolar gyre. By examining

284 the vertical profile of EKE in these different regions, we aim to identify the dynamics that controls
 285 the eddy vertical structure.

286 *a. Comparison to the Vertical Modes*

289 Vertical profiles of EKE in the four selected regions are shown in Fig .4. The EKE decays
 294 rapidly with depth in the upper ocean and gradually approaches a constant in the deep ocean. The
 295 barotropic component (i.e., the depth-independent flat-bottom mode) accounts for about 78% of
 296 the total EKE in the circumpolar current region and about 50% in the other three regions.

297 The vertical structure of EKE is compared to the structure predicted by the EBT mode (Section
 298 2a),

$$E_{\text{EBT}} = E_0 \Phi_{\text{EBT}}^2, \quad (14)$$

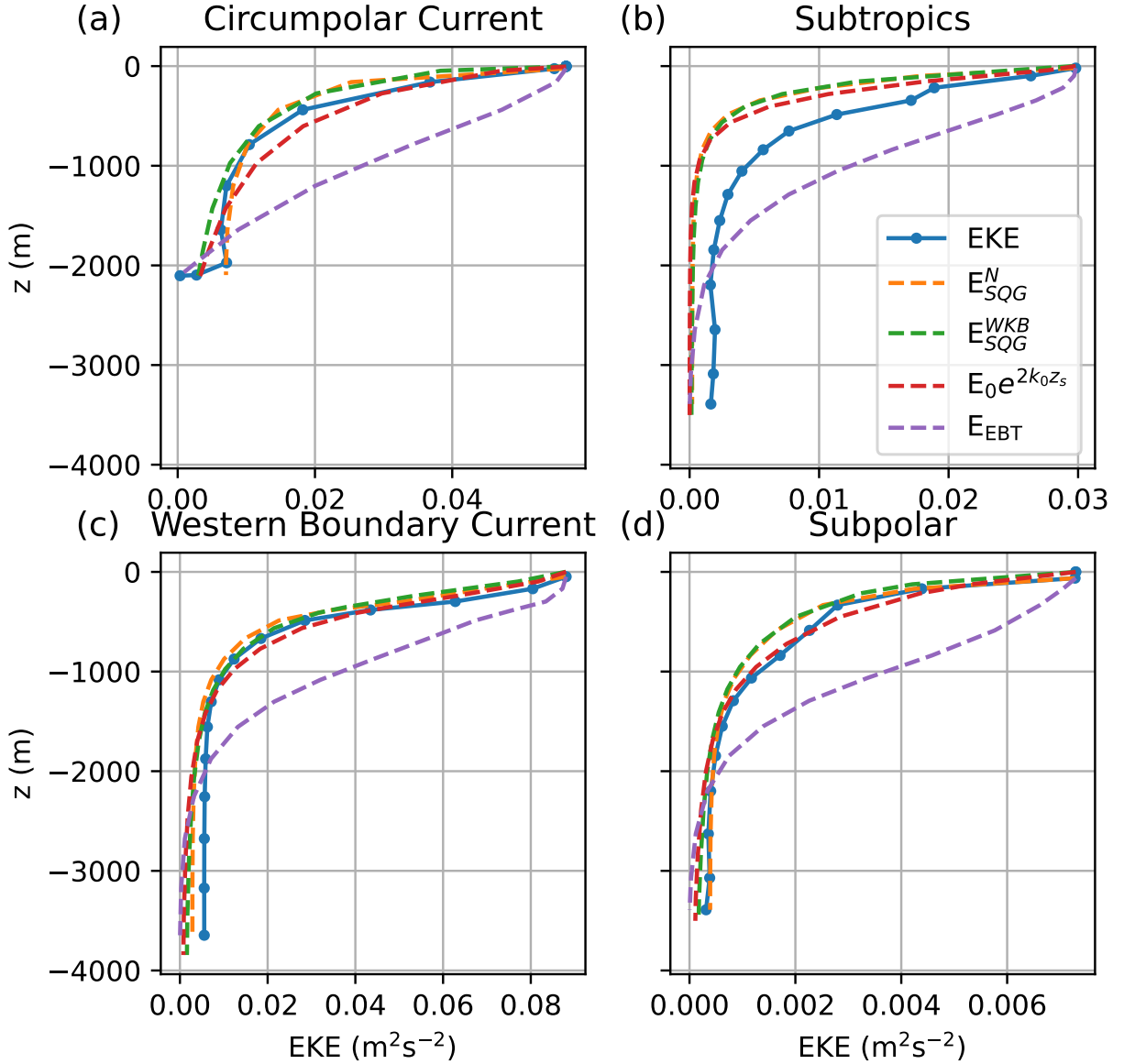
299 where E_0 is the surface EKE. The square is taken because Φ_{EBT} describes the vertical structure of
 300 eddy velocity [see equation (2)].

301 The profile of E_{EBT} is shown by the purple dashed line in Fig. 4. The EBT mode is surface-
 302 intensified, but it decays more slowly with depth than the diagnosed EKE. Furthermore, the EBT
 303 mode has zero vertical gradient at the surface due to its boundary condition in equation (5), whereas
 304 the EKE has a strong vertical gradient near the surface. Another limitation is that the magnitude of
 305 the EBT mode is zero at the bottom, but the EKE can be significant at the bottom even with strong
 306 gradients in the bottom topography.

307 The vertical gradient of eddy velocity near the surface indicates that the surface-layer PV plays an
 308 important role in the vertical structure of EKE, thus motivating us to compare the vertical structure
 309 of EKE to the SQG mode. The WKB solution of the SQG mode equation (10) gives the vertical
 310 structure of the SQG mode at each wavenumber, $\hat{\psi}_s^{\text{WKB}}$. If we know the surface streamfunction
 311 spectrum, $\hat{\psi}_0$, the vertical structure of EKE reproduced by the SQG mode, $E_{\text{SQG}}^{\text{WKB}}$, is

$$E_{\text{SQG}}^{\text{WKB}} = \frac{1}{2} \sum_k k^2 |\hat{\psi}_s^{\text{WKB}}|^2 = \frac{1}{2} \sum_k k^2 |\hat{\psi}_0|^2 e^{2kz_s}. \quad (15)$$

312 The green dashed lines in Fig. 4 show the WKB solution of the SQG mode, $E_{\text{SQG}}^{\text{WKB}}$, where
 313 $\hat{\psi}_0 = g\hat{\eta}/f$ is estimated from Fourier transform of the SSH field, η , within the four regions indicated
 314 by the blue boxes in Fig. 3a. To check the accuracy of the WKB solution, we also compute the



287 FIG. 4. Vertical profiles of diagnosed EKE (solid blue lines with dots) in the four regions shown in figure 3.
 288 The four regions are located in the (a) circumpolar current, (b) subtropical gyre, (c) western boundary current,
 289 and (d) subpolar regions. Dashed orange and green lines are the numerical and WKB solutions of the SQG
 290 mode, respectively, summed over horizontal wavenumbers of the surface EKE spectrum. Red dashed line is the
 291 WKB solution of the SQG mode at the energy-containing scale. Purple dashed line is the vertical structure of
 292 the EBT mode.

315 numerical solution of $\hat{\psi}_s$. The numerical solution of SQG EKE, E_{SQG}^N , is plotted as the orange
 316 dashed line, which is close to the WKB solution. The SQG mode captures the near exponential

317 decay of EKE well in all the regions, with the exception of the subtropics, where EKE decays
 318 slower than the SQG mode (though faster than the EBT mode). The discrepancy in the subtropics
 319 indicates a nonnegligible role of interior modes, equation (9). Overall, the SQG mode matches
 320 the vertical structure of EKE better than the EBT mode. This result suggests that the vertical
 321 structure of EKE is mainly controlled by the surface PV, in which case the vertical structure can
 322 be reconstructed using the SQG mode as described by equations (8). This result is consistent with
 323 previous studies showing how the eddy vertical structure can be reconstructed by the SQG mode
 324 in realistic ocean simulations (Klein et al. 2009; Isern-Fontanet et al. 2008; Qiu et al. 2016, 2020).

325 *b. Relating to the Energy-Containing Scale*

326 Reconstruction of the vertical structure based on the SQG mode, equation (15), requires knowl-
 327 edge of the surface energy spectrum, $k^2|\hat{\psi}_0|^2$, which is unavailable in coarse-resolution simulations.
 328 The surface energy spectrum is usually dominated by a peak, which indicates the energy-containing
 329 scale (surface energy spectra in the four regions are shown in Fig. 5). This feature suggests that
 330 the eddy vertical structure may also be dominated by the energy-containing eddy. The energy-
 331 containing wavenumber, k_0 can be estimated following Thompson and Young (2006) and Zhang
 332 and Wolfe (2022),

$$k_0 = \sqrt{\frac{\langle |\nabla\eta'|^2 \rangle}{\langle \eta'^2 \rangle}}, \quad (16)$$

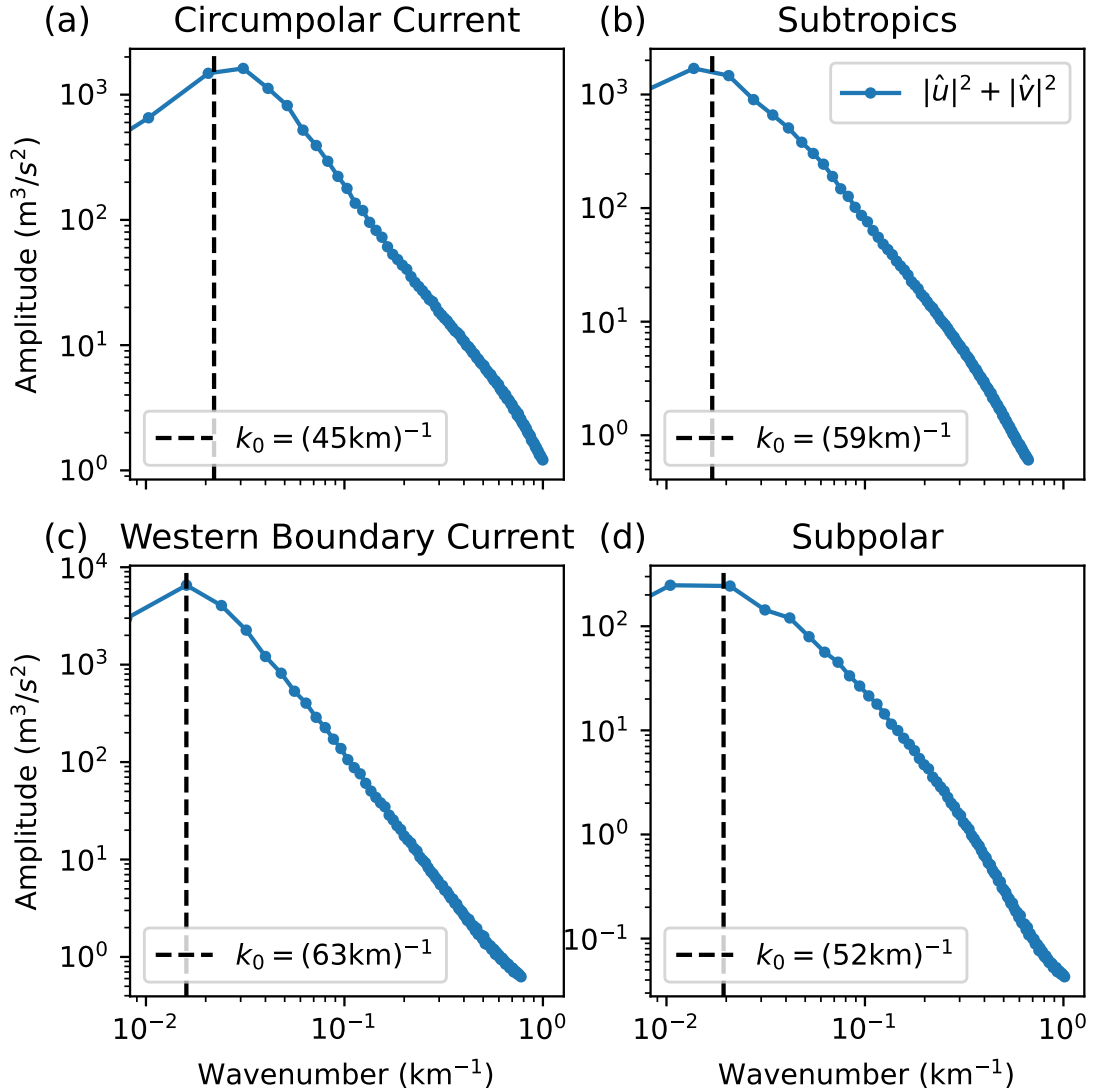
333 where η' is the spatial SSH anomaly, and $\langle \rangle$ indicates a spatial average over each of the four box
 334 regions in Fig. 3.

340 The k_0 estimated by equation (16) is shown by the black dashed line in Fig.5. This estimate is
 341 generally close to the peak of the energy spectrum. We then estimate the SQG mode structure at
 342 the energy-containing scale,

$$E_{\text{SQG}}^{k_0} = E_0 e^{2k_0 z_s}, \quad (17)$$

343 which can be calculated at each grid point without Fourier analysis.

344 The vertical structure given by equation (17) is shown by the red dashed line in Fig. 4. It works
 345 similarly well as the SQG solution based on the full energy spectrum, meaning that the vertical
 346 structure of EKE can be represented by the SQG mode structure at the energy-containing scale.



335 FIG. 5. (a)-(d) 1D surface kinetic energy spectrum (blue lines with dots) in the four regions shown in figure 3.
 336 The spectrum, $|\hat{u}|^2 + |\hat{v}|^2$ is calculated by Fourier transforming the 2D instantaneous velocity fields in $8.7^\circ \times 8.7^\circ$
 337 windows and then averaged over 500 days. The 2D spectrum is then azimuthally integrated to obtain the 1D
 338 spectrum. Black dashed line indicates the energy-containing wavenumber k_0 , estimated from (16) at the center
 339 of the four regions.

347 Equation (17) also indicates a relation between the horizontal and vertical scales of EKE. Here
 348 we measure the vertical scale as the e-folding depth, h_e , of the eddy velocity (i.e., the square root

349 of EKE). From equation (17), we can also estimate the e-folding depth of the SQG mode, h_0 ,

$$\int_{-h_0}^0 \frac{N}{|f|} dz = k_0^{-1}, \quad (18)$$

350 which is the deformation depth of the energy-containing wavenumber k_0 (Pierrehumbert and
351 Swanson 1995). If equation (17) is a good approximation of the EKE vertical structure, h_0 should
352 be equal to h_e .

353 The e-folding depth, h_e , and equivalent energy-containing depth, h_0 , are compared in the merid-
354 ional section in Fig. 3b. They compare well to each other in the extra-tropical regions (poleward of
355 20°), which is consistent with the good comparison between the EKE vertical structure and SQG
356 mode in these regions in Fig. 4. In the tropics, h_0 decreases to zero toward the equator due to
357 the decreasing magnitude of Coriolis parameter, $|f|$, in equation (18), while h_e remains around
358 1000-2000m. The large fluctuations of h_e in the tropics might be due to the spatial variability of
359 strong undercurrent and equatorial waves.

360 The comparison between h_e and h_0 at other meridional sections is similar to that in Fig. 3b.
361 The SQG mode captures the vertical structure of EKE well in the extra-tropical regions, where
362 the eddy horizontal and vertical scales are coupled in the way described by equation (18). The
363 e-folding depth for the eddy velocity is generally shallower than a half of the water depth in the
364 extra tropics, indicating that eddies are shallow. The SQG mode does not capture the vertical
365 structure of EKE well in the tropics. Fig. 3a shows that the kinetic energy pattern is wave-like
366 in the tropics, indicating that EKE is dominated by linear waves there, while in the extra tropics,
367 the flow field contains abundant coherent vortices, indicating the dominance of nonlinear eddies.
368 Previous studies have shown that the eddy flux is dominated by linear waves and nonlinear eddies
369 in the tropics and midlatitude ocean, respectively, leading to different scalings of eddy mixing in
370 these regions (Klocker and Abernathy 2014; Zhang and Wolfe 2022). We expect that equation
371 (17) is effective in describing the vertical structure of EKE in the midlatitude ocean.

372 **5. Why is the Vertical Structure SQG-like?**

373 In section 4, we have seen that the EKE structure tends to be SQG-like. Here, we discuss
374 the underlying physics by showing: (i) the EKE profile is consistent with the distributions of the
375 eddy PV and large-scale meridional PV gradient; (ii) the surface meridional PV gradient yields

376 baroclinic instability that produces surface-trapped unstable modes; (iii) the kinetic energy created
377 by baroclinic instability at small scales cascades toward the energy-containing scale in the form of
378 surface-trapped mode, resulting in an SQG-like EKE vertical structure.

379 *a. PV Structure*

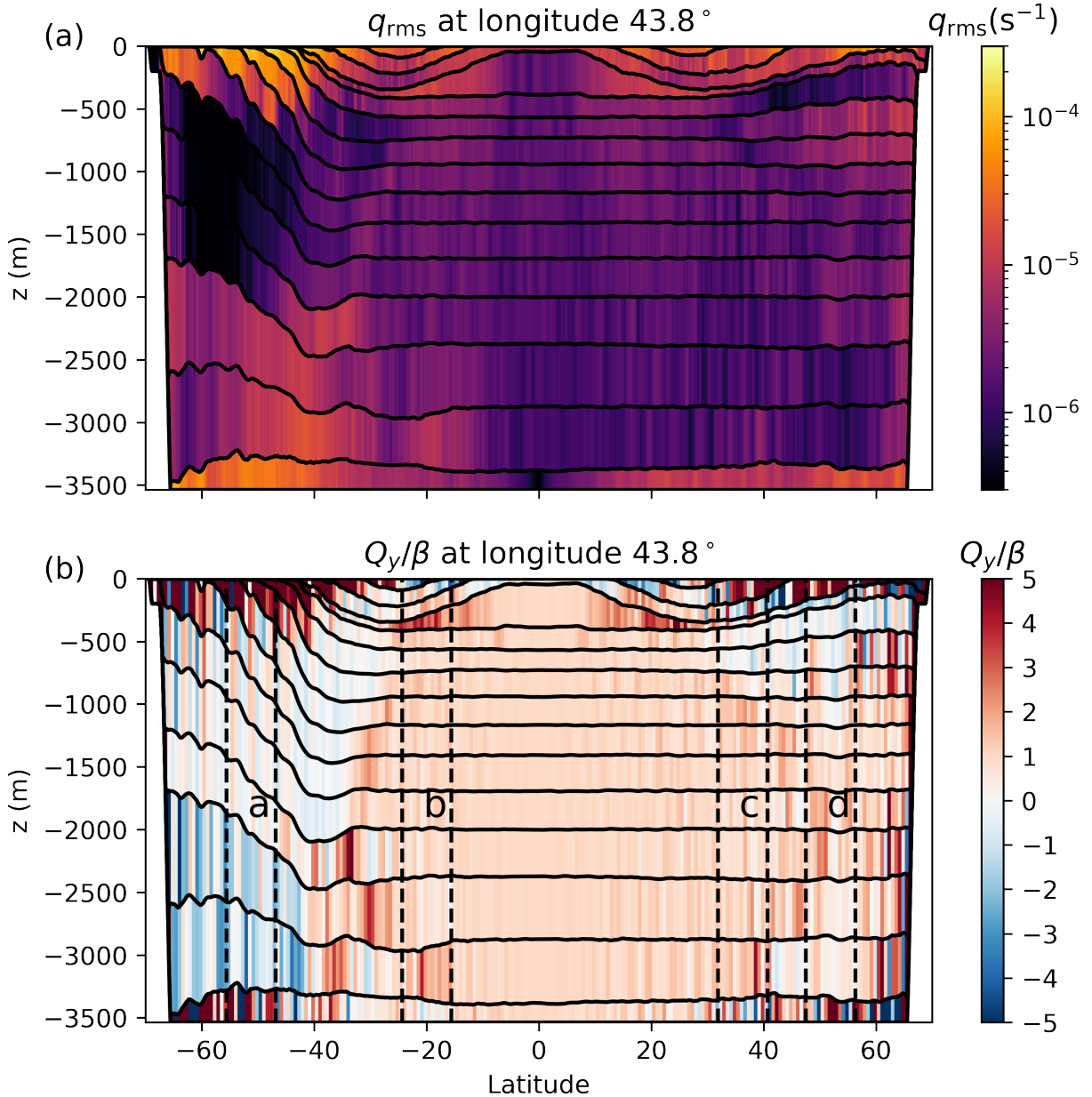
380 SQG prescribes zero interior PV anomaly. To examine this assumption, the rms eddy PV, q_{rms} ,
381 is computed as

$$q_{\text{rms}} = \sqrt{q'^2}, \quad (19)$$

382 where q is the QG PV, estimated by equation (B1) in Appendix B. Fig. 6a shows the distribution
383 of the rms eddy PV at the same meridional section as Fig. 3b. The eddy PV peaks at the surface
384 layer and becomes about an order of magnitude smaller in the interior layers, which is consistent
385 with the SQG-like EKE structure in the midlatitudes. In the subtropics ($10^\circ - 25^\circ$), the PV also
386 intensifies at about 400 m, which might be why the EKE structure is less SQG-like in these regions.

387 The distribution of eddy PV is associated with the large-scale meridional PV gradient, Q_y ,
388 structure, shown in Fig. 6b. The meridional PV gradient is estimated from equation (C3) in
389 Appendix C for the layered shallow water model. The magnitude of meridional PV gradient peaks
390 at the surface due to the isopycnal outcropping. The interior PV gradient is weak, especially in
391 the upper 1000 m in the mid- and high-latitudes (latitude poleward of 25°). The weak interior
392 PV gradient is likely due to the isopycnal mixing by eddies, which tend to homogenize the PV in
393 the interior (Holland and Rhines 1980; Rhines and Young 1982). In the circumpolar current, the
394 magnitude of PV gradient also intensifies in the near-bottom layers, which is consistent with the
395 intensification of eddy PV in these regions. In the subtropics, the PV gradient also peaks at about
396 400 m due to the flattening of isopycnals at the interior pycnocline. This pronounced interior PV
397 gradient is likely the cause of the strong subsurface eddy PV and the deviation of EKE profile from
398 SQG in the low latitudes. Quantitative analyses of the impact of PV gradient on the eddy vertical
399 structure is given in the next section.

404 In addition to variations of magnitude in the vertical, the meridional PV gradient also tends
405 to change sign from surface to the interior. In the mid- and high-latitudes, the meridional PV
406 gradient is positive at the surface layer, negative at layers below surface, and positive again in the
407 deep ocean. In the subtropics, the PV gradient is negative at the surface layer and positive in the



400 FIG. 6. Meridional and vertical distribution of (a) the rms eddy PV and (b) the meridional PV gradient
 401 normalized by β at the longitude indicated by the blue dashed line in Fig. 3a. Black solid lines are the isopycnals
 402 in the model. Black dashed lines with characters a,b,c,d indicate the latitude range of the four regions shown in
 403 Fig. 3. Note that a and c are not in the same longitude as this meridional section.

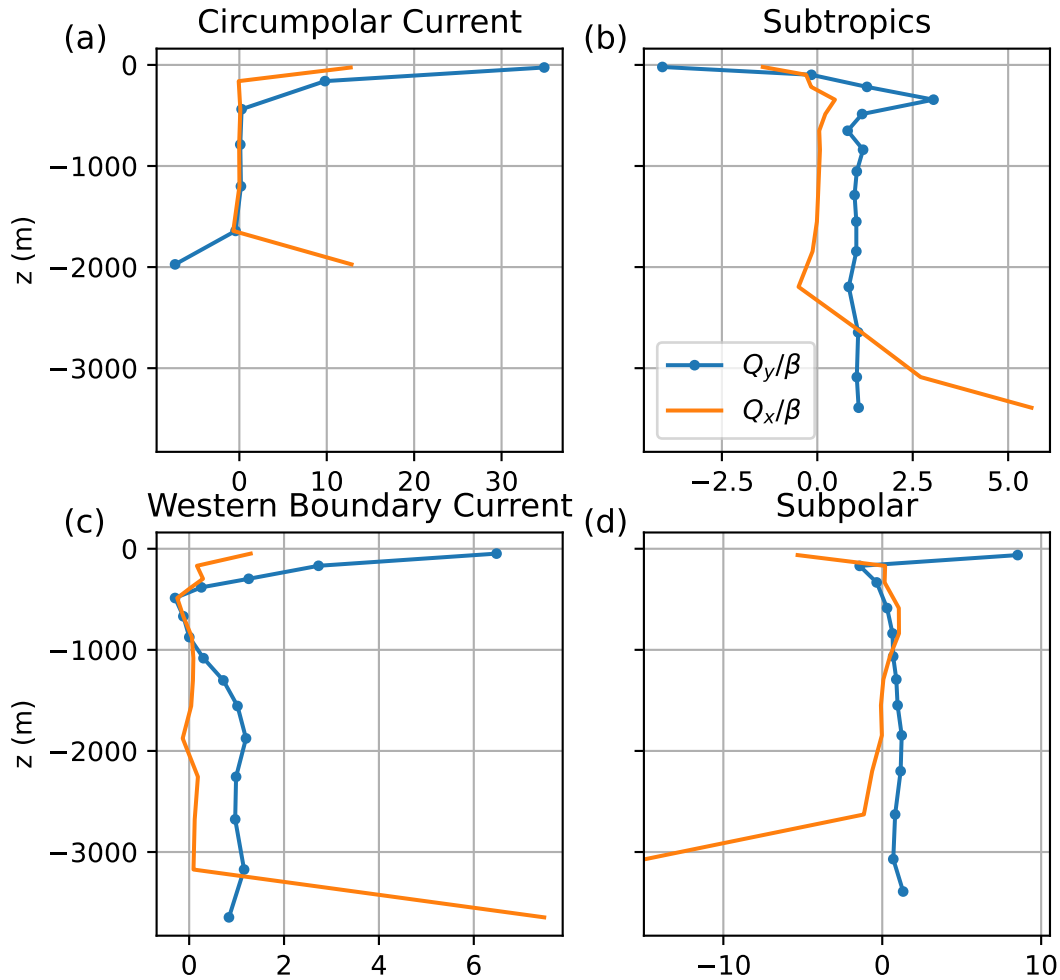
408 interior. A similar distribution of the meridional PV gradient is also found by Tulloch et al. (2011)
 409 in the schematic of their figure 2, which is based on reanalysis climatology. However, the positive

410 PV gradient is more confined near the surface in the midlatitude regions in our simulation than in
411 Tulloch et al. (2011). This feature is found to be common in the mode water regions (e.g., western
412 boundary current extension and Southern Ocean) by Capet et al. (2016) using observations. These
413 regions tend to have weak stratification layers right above the main thermocline, which squeezes the
414 positive PV gradient to the surface and creates negative meridional PV gradient below it, consistent
415 with the midlatitude PV gradient distribution in the simulation.

416 *b. Linear Stability*

417 The meridional PV gradient is often found to play a crucial role in oceanic baroclinic instability,
418 which is an important energy source for mesoscale eddies (Smith 2007; Tulloch et al. 2011; Capet
419 et al. 2016). Baroclinic instability occurs when the background horizontal PV gradient changes
420 sign in the vertical, which is a typical feature of the meridional PV gradient shown in Fig. 6b.

423 We analyze baroclinic stability in the four regions discussed in section 4. The vertical profiles
424 of the meridional and zonal PV gradients in the four regions are shown in Fig. 7. Fig. 8 shows the
425 distribution of the growth rate, σ , of unstable modes, which are solved from the eigenvalue problem
426 described by equation (C6) in Appendix C. Fig. 9 shows the vertical structure of the most unstable
427 mode, indicated by the cyan point in Fig. 8. In the circumpolar current, the interior PV gradients are
428 about ten times smaller than the surface and bottom gradients. The surface and bottom meridional
429 PV gradients are opposite to each other, which gives rise to unstable modes at scales larger than
430 the deformation radius. The vertical structure of the most unstable mode intensifies at both surface
431 and bottom, which is a typical feature of the Eady-type instability arising from the interaction
432 between the surface and bottom edge waves (Eady 1949). In the other three regions, both the
433 meridional and zonal PV gradient changes sign near the surface, and the meridional PV gradient is
434 generally stronger than the zonal gradient. The most unstable mode occurs at scales smaller than
435 the deformation radius in these three regions. The vertical structure of the most unstable mode
436 is surface-intensified, indicating a Charney-type instability arising from the interaction between
437 surface edge waves and interior Rossby waves (Charney 1947; Tulloch et al. 2011; Capet et al.
438 2016). In the subtropics, the unstable mode also intensifies at around 400m, which is associated
439 with the subsurface local maximum of the meridional PV gradient. This PV gradient maximum

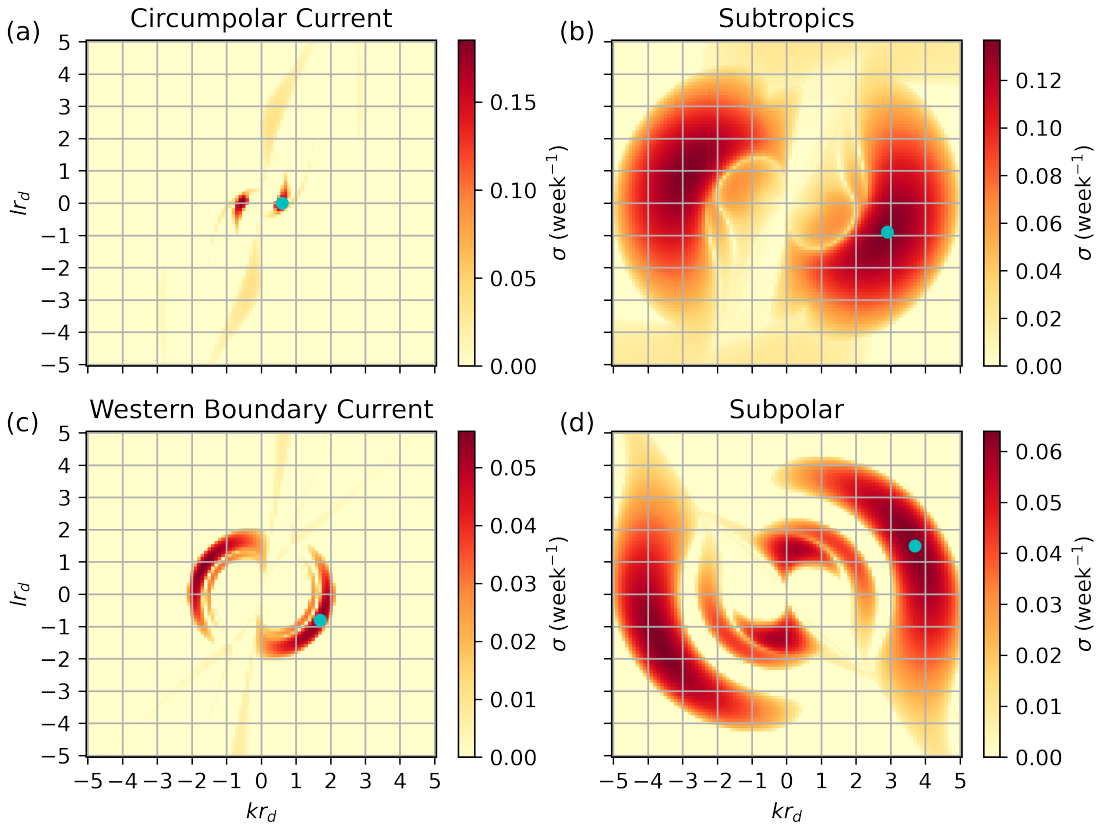


421 FIG. 7. (a)-(d) Vertical profiles of meridional (blue lines with dots at the layer centers) and zonal (orange lines)
 422 PV gradient normalized by β in the four regions shown in Fig. 3.

440 occurs at the top of the pycnocline where isopycnals start to become flat at about 400m depth in
 441 the column labeled by b in Fig. 6.

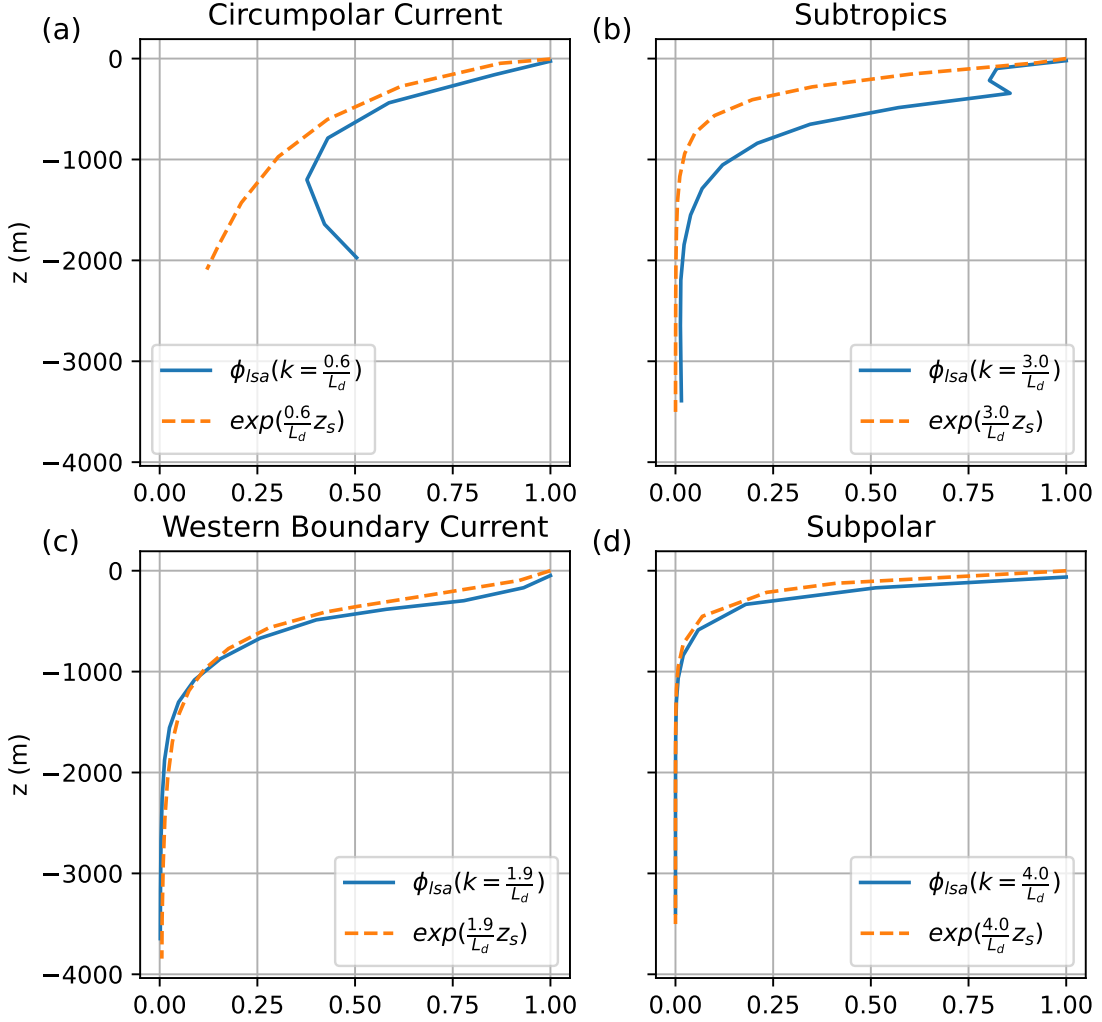
442 In the western boundary current and subpolar regions, although the meridional PV gradient also
 443 changes sign at 500–1000 m depth, nearly all unstable modes are surface-intensified in these two
 444 regions (not shown), indicating that the instability is always associated with surface edge waves.
 445 The Rossby wave propagates eastward in the negative PV gradient layers and westward in the
 446 positive PV gradient layers below (the zonal mean flow is eastward above 1000 m and becomes
 447 weak below), so they cannot couple to each other due to the mismatch between their zonal phase

448 speeds. Consequently, the sign change of PV gradient at 500–1000 m does not lead to the Phillips
 449 type instability in the interior (Phillips 1954).



450 FIG. 8. (a)-(d) Growth rate of unstable modes as a function of zonal and meridional wavenumbers, k_x and
 451 k_y , respectively, that are normalized by the deformation radius in the same four regions as in Fig. 3. Cyan point
 452 indicates the most unstable mode.

456 The vertical structure of the most unstable mode is compared to the SQG mode at the same
 457 horizontal wavenumber in Fig. 9. A resemblance between the unstable mode and the SQG mode
 458 is found in the western boundary current and subpolar regions, consistent with the comparison
 459 between the SQG mode and the vertical structure of EKE. In the subtropics, the unstable mode is
 460 similar to the SQG mode, with the exception of its subsurface intensification, likely attributed to
 461 the intensified meridional PV gradient at around 400 m due to the pycnocline. Such significant
 462 subsurface PV gradient might also contribute to the deviation of the vertical structure of EKE from
 463 the SQG mode in this region (Fig. 4b). In the circumpolar current, the SQG mode captures the
 464 vertical structure of unstable mode in the upper ocean, but fails to capture the bottom intensification



453 FIG. 9. (a)-(d) Vertical structure of the most unstable mode (blue solid line) indicated by the cyan point in
 454 Fig. 8. Orange dashed line is the normalized vertical structure of the SQG mode at the same wavenumber as the
 455 unstable mode.

456 of the unstable mode. Conversely, the vertical structure of EKE only shows a slight intensification
 457 near the bottom and appears more like the SQG mode than the unstable mode in this region
 458 (Fig. 4a). This discrepancy is likely due to the strong damping of EKE by friction at the bottom,
 thereby reducing the bottom intensification of EKE.

459 The resemblance between the unstable modes and SQG mode is attributed to the impact of
 470 the strong surface meridional PV gradient, which gives rise to strong surface edge waves that
 471 play a more important role in the vertical structure of unstable modes than the interior Rossby

472 waves. While the stability analysis is based on linear equations and local background states, it
 473 offers insights into the vertical structure of EKE. The relationship between the EKE and baroclinic
 474 instability will be further discussed in the subsequent section.

475 *c. Role of the Energy Cascade*

476 The linear stability analysis does not account for the energy cascade due to nonlinear interactions.
 477 We here diagnose the kinetic energy budget to identify the role of nonlinear advection in the eddy
 478 vertical structure. The layer-wise KE equation is

$$\frac{\partial \text{KE}_n}{\partial t} = -\mathbf{u}_n \cdot (\mathbf{u}_n \cdot \nabla \mathbf{u}_n) - \mathbf{u}_n \cdot \nabla M_n + \mathbf{u}_n \cdot \mathbf{F}_n, \quad (20)$$

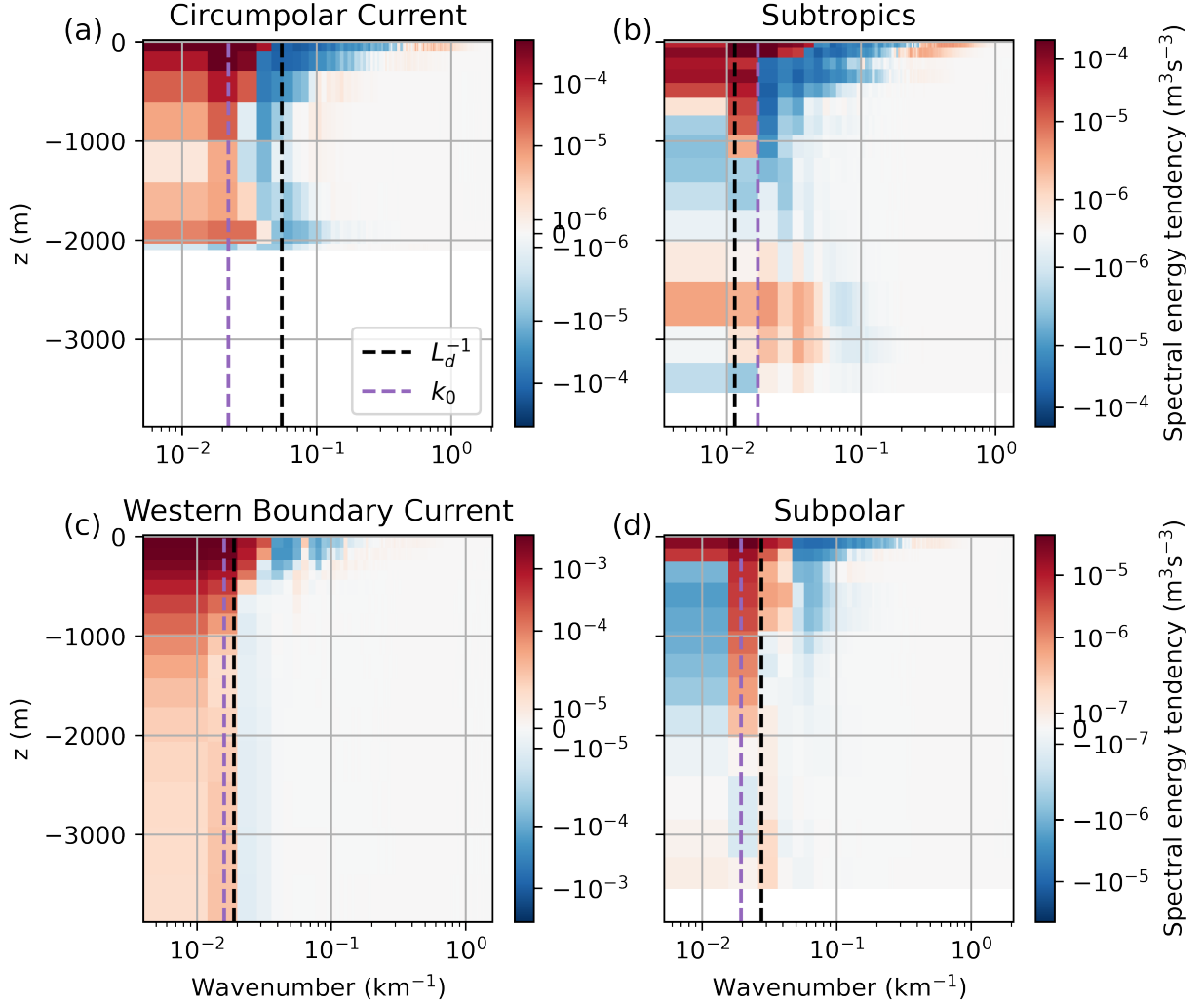
479 where M_n is the Montgomery potential, \mathbf{F}_n contains the wind stress and bottom friction, as well as
 480 vertical and horizontal viscous friction.

481 The first term on the RHS of equation (20) is the KE tendency due to nonlinear advection, which
 482 is not accounted for in the linear stability analysis. The role of nonlinear advection is examined by
 483 decomposing it in spectral space. The cospectrum of the nonlinear advection, T_n , is calculated as

$$T_n = -\text{Re} \left[\overline{\widehat{\mathbf{u}}_n^* \cdot (\mathbf{u}_n \cdot \nabla \mathbf{u}_n)} \right], \quad (21)$$

484 where $\text{Re}(\cdot)$ indicates taking the real part, $(\cdot)^*$ is the complex conjugate, $\bar{\cdot}$ indicates a 500-day
 485 average.

486 The advection term, T_n , quantifies the spectral tendency of KE due to the KE cascade between
 487 horizontal wavenumbers. The positive and negative values of $T_n(k)$ indicate that energy cascade
 488 deposits and removes KE, respectively, for eddies at the corresponding wavenumber k . The time
 489 tendency term on the LHS of equation (20) is close to zero when taking a long-time average.
 490 In this case, the energy cascade balances the net energy source or sink due to the work by the
 491 horizontal pressure gradient [second term on the RHS of equation (20)], forcing and dissipation
 492 [third term on the RHS of equation (20)] at each wavenumber. The work by the horizontal pressure
 493 gradient includes the contribution from the divergence of 3D energy transport by pressure and the
 494 conversion of potential energy (PE) to KE due to baroclinic instability (Capet et al. 2008).



495 FIG. 10. Cospectrum of the advection term of KE, T_n , as a function of horizontal wavenumber and depth in the
 496 four regions shown in Fig. 3. Blue color indicates that nonlinear advection removes KE from the corresponding
 497 wavenumber, which balances the KE source by other terms on the RHS of the KE equation (20), while red
 498 color means that nonlinear advection supplies KE to balance the KE sink by the other terms. Black dashed
 499 line indicates the inverse of the Rossby deformation radius. Purple dashed line indicates the energy-containing
 500 wavenumber, k_0 . Note the different color range for each panel.

501 Fig. 10 shows the distribution of T_n at horizontal wavenumber and depth in the four regions. The
 502 red and blue colors indicate that energy cascade deposits and removes KE, respectively, for eddies
 503 at the corresponding wavenumber. The vertical structure of T_n is generally surface intensified
 504 and decays faster with depth at smaller scales (larger wavenumbers), which is consistent with

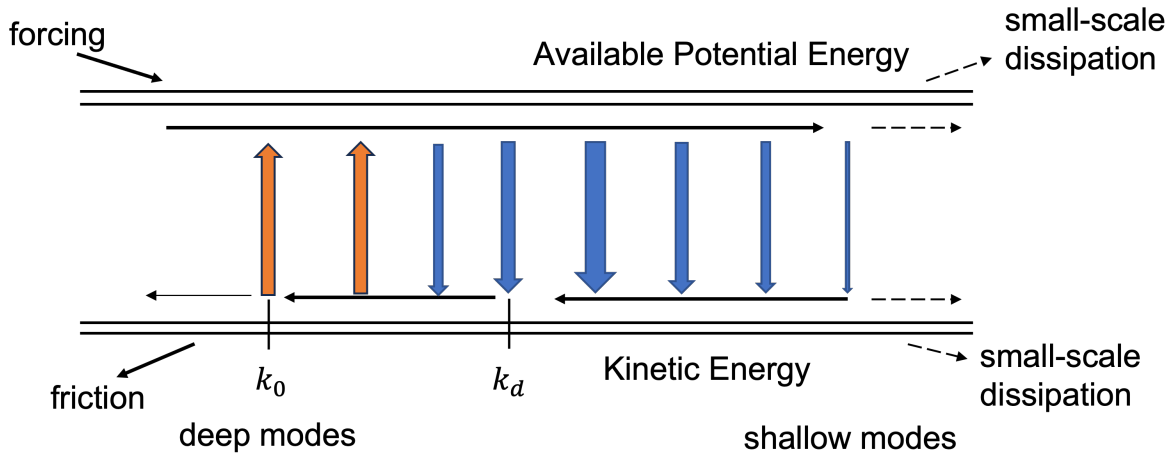
505 characteristics of the SQG mode. In the circumpolar current, the energy cascade removes energy
506 at around the deformation radius. This energy sink due to energy cascade intensifies at both the
507 surface and bottom, which is consistent with the unstable mode of the Eady instability at this
508 region (section 5b), indicating that the energy cascade balances the baroclinic instability at these
509 wavenumbers. At the other three regions, the energy cascade mainly removes energy from scales
510 smaller than the deformation radius. This energy sink concentrates near the surface, which is likely
511 to balance the energy source due to the Charney baroclinic instability in these regions. There is also
512 an energy sink at small wavenumbers at around 1000 m in the subtropical and subpolar regions,
513 though it is about an order smaller than the value of T_n at surface. This sink is likely to balance the
514 baroclinic instability at small wavenumbers in these two regions (see the growth rate distribution
515 in Fig. 8).

516 The energy cascade deposits energy at scales larger than the deformation radius in all the four
517 regions. This energy source due to energy cascade maximizes at the energy-containing scale (purple
518 dashed line in Fig. 10). This source is balanced by energy conversion from KE to PE and friction
519 (not shown). These results show that the energy cascade transfers energy generated by baroclinic
520 instability at scales close to or smaller than the deformation radius to the energy-containing eddies,
521 where kinetic energy is consumed by conversion to potential energy and friction.

522 The energy cycle shown by Fig. 10 is illustrated by the schematic in Fig. 11, which is motivated
523 by a similar schematic in Roulet et al. (2012). The forcing inputs PE to circulation at the large
524 scales. The PE is converted to KE at scales that are close to or smaller than the deformation radius
525 through baroclinic instability. The baroclinic instability is generally dominated by the surface PV
526 gradient, which gives rise to surface-trapped unstable modes. These unstable modes cascade KE
527 from small scales to large scales through their nonlinear interactions until the cascade is halted at
528 the energy-containing scale. Consequently, the vertical structure of EKE is dominated by the mode
529 structure at the energy-containing scale, which is deeper than the original unstable modes but still
530 remains surface-trapped.

540 **6. A Scale-Aware Parameterization**

541 Section 4 shows that SQG modes play an important role in setting the vertical structure of EKE.
542 How can this finding inform the parameterization of the eddy vertical structure? A crucial property



531 FIG. 11. Energy schematic modified from Roulet et al. (2012). The forcing supplies available potential energy
 532 (upper horizontal lines). The available potential energy cascades to smaller scales and is then converted to kinetic
 533 energy (lower horizontal lines) through baroclinic instability (blue arrows) at a broad range of horizontal scales
 534 that are close to or smaller than the deformation radius, the inverse of k_d . The unstable modes arising from
 535 the instability are surface-trapped, which decay faster with depth at smaller scales. The kinetic energy of these
 536 unstable modes cascades from small scales (shallow modes) to large scales (deep modes) until the cascade is
 537 halted at the energy-containing scale, the inverse of k_0 . Part of the kinetic energy is dissipated by the friction and
 538 the other part is converted back to available potential energy (orange arrows) at around the energy-containing
 539 scale.

543 of the SQG mode is the coupling of its vertical and horizontal scales. As is shown in the analytical
 544 expression (10), smaller horizontal scale eddies, which have a larger horizontal wavenumber, decay
 545 more rapidly with depth than larger eddies. In the context of eddy parameterization, the focus is
 546 on representing the subgrid EKE that is unresolved by the model. As the model grid spacing is
 547 refined, the scale of unresolved eddies becomes smaller, resulting in a shallower vertical structure
 548 of subgrid EKE. This result suggests that the parameterization of the vertical structure of subgrid
 549 EKE should depend explicitly on the model grid spacing.

550 To examine the scale dependence of the eddy vertical structure, we employ high-pass spatial
 551 filters on the eddy velocity fields to compare the vertical structure at different horizontal scales.
 552 Fig. 12 shows the normalized vertical structures for eddies smaller than $2\pi/0.25^\circ$, $2\pi/0.5^\circ$, and
 553 $2\pi/1^\circ$, represented by the solid blue, orange, and green lines, respectively. The vertical structure

554 of EKE becomes shallower as the horizontal scale becomes smaller. This finding is consistent with
 555 the prediction by SQG, highlighting the scale dependence of the eddy vertical structure.

556 To represent the scale-dependent eddy vertical structure at different model resolutions, we propose
 557 a scale-aware parameterization of the normalized EKE profile, E_p ,

$$E_p = e^{2k_g z_s}, \quad (22)$$

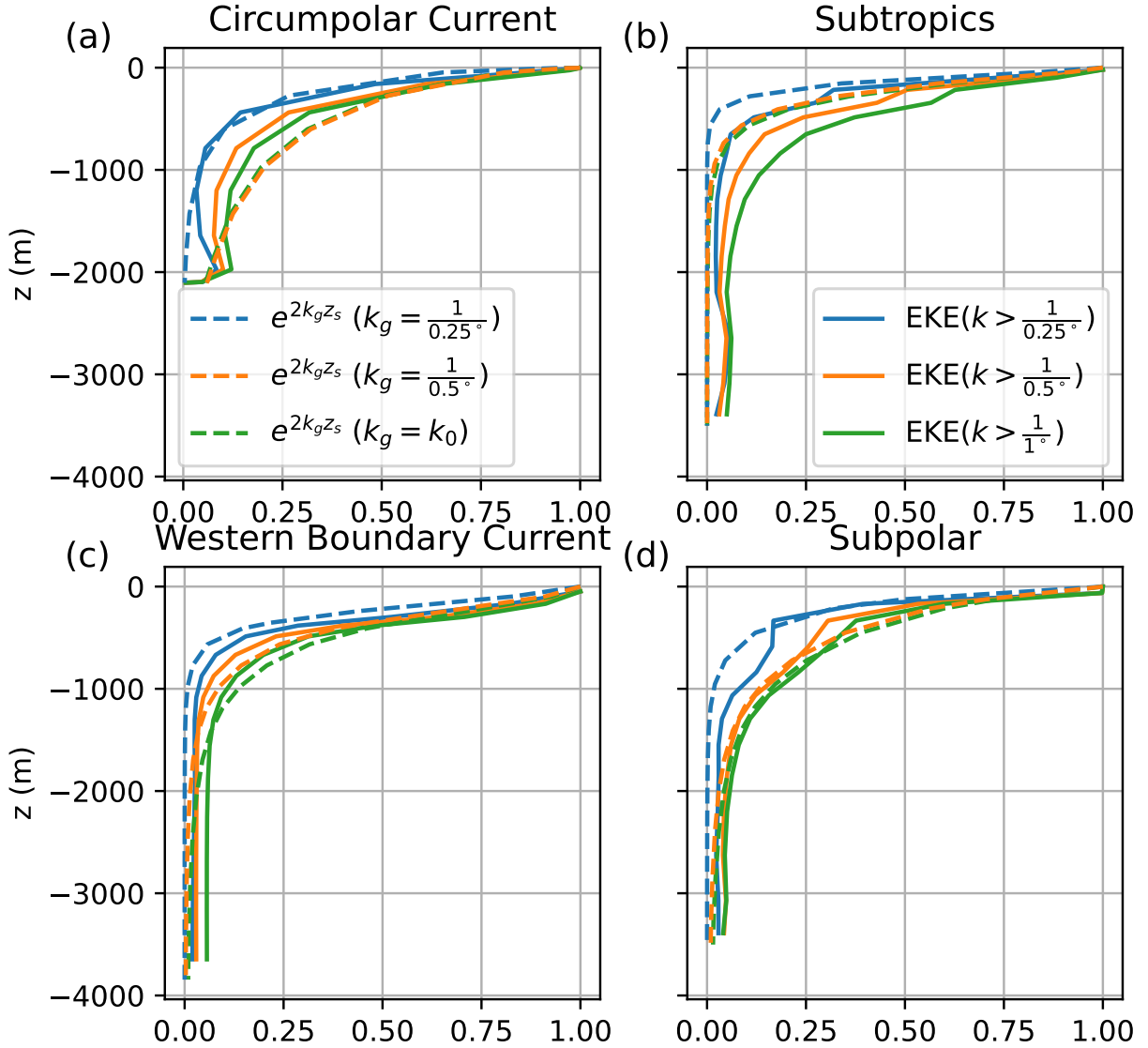
558 with

$$k_g = \max(k_0, c/\Delta), \quad (23)$$

559 where Δ is the model grid spacing, and c is a dimensionless constant, which will be a tuning
 560 parameter. The ratio, c/Δ , is proportional to the largest wavenumber resolved by the model with
 561 grid spacing Δ . The constant c is on the order of 1 and determined by the minimum number
 562 of grid points needed to resolve a wavelength ($c = 1$ means that the model needs about 6 grid
 563 points to resolve a wavelength since $2\pi/6\Delta \approx 1/\Delta$). If $k_0 > c/\Delta$, that means the energy containing
 564 scale is unresolved by the model, so the vertical structure of the subgrid EKE is dominated by the
 565 energy-containing wavenumber k_0 . If $k_0 < c/\Delta$, the energy-containing scale is resolved, so the
 566 vertical structure of subgrid EKE will be dominated by the largest resolved wavenumber (i.e., c/Δ)
 567 instead.

568 To evaluate the effectiveness of the parameterization (23), we conduct tests by varying Δ to
 569 0.25° , 0.5° , and 1° and assume $c = 1$, which means we assume a minimum of 6 grid points is
 570 required to resolve an eddy. The parameterization profiles (22) with 0.25° , 0.5° , and 1° are shown
 571 by the dashed blue, orange, and green lines in Fig.12, respectively. Compared with the solid
 572 blue, orange, and green lines in Fig.12, which represent the vertical structure of subgrid EKE in
 573 0.25° , 0.5° , and 1° model grid spacings, respectively, the parameterization well captures the scale
 574 dependence of the eddy vertical structure. The parameterization profiles look similar to the vertical
 575 structure of subgrid EKE at different resolutions, with the exception for the subtropics where the
 576 parameterization tends to decay faster than the subgrid EKE. This result is consistent with the
 577 comparison between the SQG mode and total EKE in Fig. 4.

578 The parameterization based on equation (22) requires the prediction of the energy-containing
 588 scale. Studies have estimated the energy-containing scale as the Rossby deformation radius (Stone



578 FIG. 12. The vertical structure of spatially filtered EKE in the four regions shown in Fig.4. Blue, orange, and
 579 green solid lines are the high-pass filtered vertical structure of EKE with cutoff wavenumber as $1/0.25^\circ$, $1/0.5^\circ$,
 580 and $1/1^\circ$, respectively. They represent the vertical structures of subgrid EKE that is unresolved by 0.25° , 0.5° ,
 581 and 1° models, assuming a minimum of six grid points is required to resolve an eddy. All EKE profiles are
 582 normalized by their surface values. Blue, orange, and green dashed lines are the parameterized vertical structure
 583 $E_p(z, \Delta)$. E_p depends on the model grid spacing Δ and the energy-containing wavenumber k_0 . The vertical
 584 structure of subgrid EKE is determined by Δ at 0.25° and 0.5° resolutions, where the energy-containing eddy is
 585 resolved, and by k_0 at 1° resolution. The parameterization captures the scale dependence reasonably well, except
 586 for an underestimation in the subtropical region.

589 1972), width of the baroclinic zone (Visbeck et al. 1997), Eady length scale (Larichev and Held
590 1995; Jansen et al. 2015), and Rhines scale (Jansen et al. 2015, 2019). Examination of these
591 theories for predicting the eddy scale is beyond the scope of this study and will be pursued in
592 forthcoming work.

593 **7. Discussion and Conclusions**

594 This study addresses the question of why ocean mesoscale eddies are surface intensified—at least
595 those realized within our idealized stacked shallow water model—with an aim to parameterize the
596 eddy vertical structure. Unlike previous studies that explain the eddy vertical structure from the
597 perspective of baroclinic modes (Wunsch 1997; de La Lama et al. 2016; Lacasce 2017; Brink and
598 Pedlosky 2020; Quan et al. 2023), we attribute the eddy vertical structure to baroclinic instability
599 and the energy cascade. The vertical structure of EKE is found to be well-represented by a single
600 SQG mode of the energy-containing scale in the extra tropics, indicating that the surface PV plays
601 a dominant role in the eddy vertical structure.

602 *a. Baroclinic instability and the surface-trapped mode*

603 The prevalence of the SQG mode is attributed to the surface-trapped baroclinic instability and
604 energy cascade. Although the model used in this study does not have surface buoyancy forcing,
605 the wind forcing induces isopycnal outcropping, leading to pronounced surface meridional PV
606 gradients. The interior PV gradient is much weaker compared with the surface PV gradient due
607 to the interior PV homogenization by eddies. Linear stability analysis shows that the surface PV
608 gradient plays a dominant role in baroclinic instability, giving rise to surface-trapped unstable
609 modes. These unstable modes are often smaller than the Rossby deformation radius, except in the
610 circumpolar current where they are close to the deformation radius. Through nonlinear interactions,
611 unstable modes transfer their kinetic energy upscale to energize mesoscale eddies, which have an
612 energy-containing scale larger than the deformation radius but retain the surface-trapped vertical
613 structure.

614 Early geostrophic turbulence theory shows that baroclinic eddies tend to transfer their energy to
615 the barotropic (depth independent) mode, and then barotropic eddies cascade their energy upscale
616 (Charney 1971; Salmon 1980). Later studies have found that ocean eddies are not fully barotropic,

617 and as a consequence, the inverse energy cascade can occur in both the barotropic and baroclinic
618 modes (Smith and Vallis 2001; Scott and Arbic 2007). In this study, we propose a different
619 interpretation of the eddy energy cycle. Instead of decomposing the energy into the barotropic
620 and baroclinic modes, we find that the energy cascade can directly occur among surface-trapped
621 modes. The vertical and horizontal scales of these surface-trapped modes are coupled—smaller
622 eddies decay faster with depth. Consequently, as eddies transfer energy to larger scales, they also
623 grow deeper, in alignment with the barotropization tendency of geostrophic turbulence (Charney
624 1971; Salmon 1980). Although eddies can become nearly barotropic if their horizontal scales are
625 an order of magnitude larger than the deformation radius, the inverse energy cascade tends to be
626 halted at a scale that is comparable to the deformation radius. As a result, the vertical structure of
627 energy-containing eddies is surface intensified, similar to the SQG mode.

628 *b. Parameterization of vertical structure based on SQG*

629 The vertical structure of EKE depends on the horizontal scale, with smaller eddies decaying
630 faster with depth. This feature suggests that the parameterization of eddy vertical structure should
631 account for the horizontal scale of unresolved eddies. As the model grid spacing becomes finer,
632 the unresolved eddies will be smaller and have a shallower vertical structure. Based on the WKB
633 solution of the SQG mode, we propose a scale-aware parameterization of the vertical structure of
634 EKE [equations (22) and (23)], building upon previous work using the SQG mode for diagnostic
635 studies of the ocean’s eddy vertical structure (e.g., Lapeyre and Klein 2006; Isern-Fontanet et al.
636 2008; Klein et al. 2009; Qiu et al. 2016, 2020). This parameterization requires the specification of
637 an eddy horizontal scale that depends on the model grid spacing. If the energy-containing scale is
638 not resolved, the vertical structure parameterization is determined by the energy-containing scale
639 itself. On the other hand, if the energy-containing scale is resolved—which may be the case in
640 eddy-permitting models now being used for climate studies (e.g., Adcroft et al. 2019)—the vertical
641 structure parameterization is determined by the largest unresolved scale that is proportional to
642 the horizontal grid spacing. This parameterization is shown to capture the vertical structure of
643 EKE filtered with different horizontal scales, so that it can be useful for both non-eddy and
644 eddy-permitting simulations.

645 Full closure of the vertical structure parameterization requires a prediction of the horizontal
646 energy-containing scale. The energy-containing scale is associated with the mechanism that halts
647 the inverse energy cascade; for example, bottom friction and the planetary vorticity gradient (Rhines
648 1975; Larichev and Held 1995). Prediction of such an eddy length scale has been the focus of many
649 studies (Larichev and Held 1995; Held and Larichev 1996; Thompson and Young 2006; Jansen
650 et al. 2015; Kong and Jansen 2017; Chang and Held 2019; Gallet and Ferrari 2020; Chang and
651 Held 2021; Gallet and Ferrari 2021).

652 The SQG mode does not fully capture the vertical structure of EKE in the lower latitudes and
653 tropics. Previous studies reveal that the scaling for eddy mixing is different between the tropics
654 and midlatitude ocean due to the dominance of linear waves (tropics) versus nonlinear eddies
655 (extra tropics) (Klocker and Abernathy 2014; Zhang and Wolfe 2022). Parameterization of the
656 eddy vertical structure in the tropics requires additional work, though eddies there are mostly large
657 enough to be well resolved by models targeted for climate simulations in the near future such as
658 Adcroft et al. (2019).

659 *c. Prospects and future work*

660 Many previous studies consider the importance of bottom topography in causing the surface
661 intensification of ocean eddies (Aoki et al. 2009; de La Lama et al. 2016; Lacasce 2017; Quan
662 et al. 2023). Bottom topography can decouple abyssal eddies from upper-ocean eddies, leading
663 to baroclinic modes with zero horizontal velocity at the bottom (Rhines 1970; Samelson 1992;
664 Hallberg 1997; Bobrovich and Reznik 1999; Tailleux and McWilliams 2001). We find that the first
665 rough-bottom mode (the EBT mode), with zero horizontal velocity at the bottom, does not describe
666 the vertical structure of EKE well in our simulation. This limitation arises from the EBT mode's
667 ignorance of the surface buoyancy anomaly, which we find to be essential for reconstructing the eddy
668 vertical structure. In fact, both the surface buoyancy and bottom topography can be incorporated
669 in the general boundary conditions, described by equation (6), of vertical modes (Lacasce 2017;
670 Yassin and Griffies 2022a). The vertical mode accounting for both effects will be explored in future
671 work.

672 The model used in this study does not have a mixed layer, which can change the quantitative
673 analyses of the instability and eddy energetics but, we expect, will not qualitatively change the

674 role of surface PV in the vertical structure. Mixed layer baroclinic instability provides another
675 important energy source for submesoscale eddies, which can cascade their energy upscale to
676 energize mesoscale eddies (e.g., Fox-Kemper et al. 2008b; Sasaki et al. 2014; Callies et al. 2016;
677 Schubert et al. 2020; Dong et al. 2020; Khatri et al. 2021). Callies et al. (2016) shows that the
678 energy generated by mixed layer instability resides in the SQG mode, where the energy cascades
679 upscale to the largest, most energetic eddies. This energy cascade is similar to our finding, with the
680 difference that the SQG mode is mainly excited by the surface Charney instability in our model.
681 The mixed-layer instability thus may play a similar role to the Charney instability in enhancing the
682 surface-trapped mode. In a more realistic numerical setup, the mixed layer and Charney instabilities
683 can coexist, with the relative importance between them depending on the depth of the mixed layer,
684 stratification, and lateral buoyancy gradient in the upper ocean (Capet et al. 2016; Zhang et al.
685 2023).

686 This study serves as a step forward to understand and parameterize the eddy vertical structure
687 by emphasizing its dependence on the horizontal scale, resulting from the impact of surface PV.
688 The parameterization, described by equation (22), is ripe to be tested in non-eddy and eddy-
689 permitting simulations after combining it with a closure of the horizontal energy-containing scale
690 (e.g., Jansen et al. 2015, 2019). We are planning to apply this vertical structure to the kinetic
691 energy backscatter parameterization that has recently been used in both idealized and realistic
692 eddy-permitting simulations (Jansen et al. 2019; Juricke et al. 2019, 2020; Yankovsky et al. 2023;
693 Chang et al. 2023). Other aspects, including the impacts of bottom topography and mixed layer,
694 will also be incorporated in this scheme to predict the eddy vertical structure in more realistic
695 situations. Such scheme will be validated by comparing to observations of full-depth eddy profile
696 (Ni et al. 2023).

697 *Acknowledgments.* We thank Alistair Adcroft, Laure Zanna, Elizabeth Yankovsky, Malte Jansen,
698 Shafer Smith and Baylor Fox-Kemper for helpful discussions. We also thank Chiung-Yin Chang,
699 Jacob Steinberg, and Matthew Lobo for comments on drafts of this manuscript. This work was
700 supported by award NA18OAR4320123 from the National Oceanic and Atmospheric Administra-
701 tion, U.S. Department of Commerce. The statements, findings, conclusions, and recommendations
702 are those of the author(s) and do not necessarily reflect the views of the National Oceanic and
703 Atmospheric Administration, or the U.S. Department of Commerce. W.Z. was also supported by
704 the NSF (OCE-2048826).

705 *Data availability statement.* The model, NeverWorld2, data set and detailed information on its
706 configuration are available at <https://doi.org/10.26024/f130-ev71> (Marques et al. 2022).

707 APPENDIX A

708 **Comparison of the Surface-Trapped Mode to the Solution in Lapeyre and Klein (2006)**

709 The orthogonal basis derived from equations (8) and (9) is different from that in Lapeyre and Klein
710 (2006). They proposed a decomposition of the eddy streamfunction ψ into a surface component
711 ψ_{sur} satisfying

$$\begin{aligned} \nabla^2 \psi_{\text{sur}} + \frac{\partial}{\partial z} \left(\frac{f^2}{N^2} \frac{\partial \psi_{\text{sur}}}{\partial z} \right) &= 0, \\ \frac{\partial \psi_{\text{sur}}}{\partial z} \Big|_{z=0} &= \frac{b_s}{f}, \\ \frac{\partial \psi_{\text{sur}}}{\partial z} \Big|_{z=-H} &= 0, \end{aligned} \quad (\text{A1})$$

712 and an interior component ψ_{int} satisfying

$$\begin{aligned} \nabla^2 \psi_{\text{int}} + \frac{\partial}{\partial z} \left(\frac{f^2}{N^2} \frac{\partial \psi_{\text{int}}}{\partial z} \right) &= q, \\ \frac{\partial \psi_{\text{int}}}{\partial z} \Big|_{z=0} &= 0, \\ \frac{\partial \psi_{\text{int}}}{\partial z} \Big|_{z=-H} &= 0. \end{aligned} \quad (\text{A2})$$

713 Here b_s is the surface buoyancy anomaly and q the PV, with the bottom boundary condition
714 specified following Lapeyre (2009).

715 The interior solution, ψ_{int} , is driven by interior PV anomalies and can be projected onto the
716 flat-bottom modes, described by equations (2) and (4). The surface solution, ψ_{sur} , is driven
717 by surface buoyancy anomalies. Although ψ_{sur} and the surface-trapped mode Φ_s [described by
718 equation (8)] share certain properties (i.e., zero interior PV anomaly and horizontal wavenumber
719 dependence), ψ_{sur} satisfies a Neumann surface boundary condition (i.e., surface buoyancy anomaly
720 is given) while Φ_s a Dirichlet surface boundary condition (i.e., surface pressure anomaly is given).
721 Consequently, ψ_{sur} is not orthogonal to the interior solution ψ_{int} . In contrast, Φ_s is orthogonal to the
722 interior modes Φ_m described by equation (9). Later studies have shown that the surface solution
723 ψ_{sur} —modified to incorporate surface pressure anomaly—is better for reproducing the vertical
724 structures of EKE and vertical velocity than the original formulation based on surface buoyancy
725 anomaly (Isern-Fontanet et al. 2008; Klein et al. 2009; Isern-Fontanet et al. 2014; González-Haro
726 and Isern-Fontanet 2014).

727 APPENDIX B

728 SQG Mode in Layered Quasigeostrophic Models

729 Eddies in the shallow water model, described in Section 3a, are analyzed based on layered
730 quasigeostrophic (QG) dynamics. The eddy streamfunction ψ can be obtained from the distribution
731 of the QG PV, q , by inverting the relation

$$\begin{aligned}
 q_1 &= \nabla^2 \psi_1 + \frac{f^2}{H_1} \frac{\psi_2 - \psi_1}{g'_1}, \\
 q_n &= \nabla^2 \psi_n + \frac{f^2}{H_n} \left(\frac{\psi_{n-1} - \psi_n}{g'_{n-1}} - \frac{\psi_n - \psi_{n+1}}{g'_n} \right), \quad n \in [2, n_{\text{max}} - 1], \\
 q_{n_{\text{max}}} &= \nabla^2 \psi_{n_{\text{max}}} + \frac{f^2}{H_{n_{\text{max}}}} \frac{\psi_{n_{\text{max}}-1} - \psi_{n_{\text{max}}}}{g'_{n_{\text{max}}-1}},
 \end{aligned} \tag{B1}$$

732 where $(\cdot)_n$ indicates the property on the n -th layer, H_n is the layer thickness, f is the Coriolis
733 parameter, $n_{\text{max}} = 15$ for our simulations, and g'_n is the reduced gravity, computed as

$$g'_n = g \frac{\rho_{n+1} - \rho_n}{\rho_0}, \tag{B2}$$

734 where $g = 10 \text{ m}^2 \text{ s}^{-1}$, ρ_n is the uniform layer density, and $\rho_0 = 1000 \text{ kg/m}^3$ is the reference density.
 735 We emphasize that n in this paper is used to label the discrete layer number in the stacked shallow
 736 water model, whereas m was introduced earlier and denotes the vertical eigenmode.

737 In matrix form, the relationship between $\mathbf{q} = [q_1, \dots, q_{n_{\max}}]^\text{T}$ and $\boldsymbol{\psi} = [\psi_1, \dots, \psi_{n_{\max}}]^\text{T}$ can be
 738 written as

$$\mathbf{q} = (\mathbf{S} + \mathbf{I}\nabla^2) \boldsymbol{\psi}, \quad (\text{B3})$$

739 where \mathbf{I} is the $N \times N$ identity matrix, and \mathbf{S} is the stretching matrix written as

$$\mathbf{S} = f^2 \begin{bmatrix} -\frac{1}{H_1 g'_1} & \frac{1}{H_1 g'_1} & 0 & 0 & \dots \\ \vdots & \vdots & \vdots & \vdots & \vdots \\ \dots & \frac{1}{H_n g'_{n-1}} & -\frac{1}{H_n g'_{n-1}} - \frac{1}{H_n g'_n} & \frac{1}{H_n g'_n} & \dots \\ \vdots & \vdots & \vdots & \vdots & \vdots \\ \dots & 0 & 0 & \frac{1}{H_{n_{\max}} g'_{n_{\max}-1}} & -\frac{1}{H_{n_{\max}} g'_{n_{\max}-1}} \end{bmatrix}$$

740 Surface buoyancy is not explicitly simulated in a stacked shallow water model. Even so, its
 741 dynamical impact is similar to that of the surface-layer PV, q_1 . The streamfunction due to SQG
 742 dynamics, $\boldsymbol{\psi}_s$, is equivalent to the streamfunction induced by the surface-layer PV,

$$\boldsymbol{\psi}_s = (\mathbf{S} + \nabla^2 \mathbf{I})^{-1} \mathbf{q}_s, \quad (\text{B4})$$

743 where $\mathbf{q}_s = [q_1, 0, \dots, 0]^\text{T}$.

744 APPENDIX C

745 Linear Stability Analysis

746 The QG PV evolution equation in a layered QG model (e.g., Vallis 2017) is

$$\frac{\partial q_n}{\partial t} + U_n \frac{\partial q_n}{\partial x} + V_n \frac{\partial q_n}{\partial x} + \mathbf{J}(\psi_n, q_n) + \mathbf{J}(\psi_n, Q_n) = 0, \quad (\text{C1})$$

747 where \mathbf{J} is the Jacobian, U and V are the background zonal and meridional velocities, and Q is the
 748 background PV estimated as

$$\mathbf{Q} = \mathbf{S}\mathbf{V}x + (\beta - \mathbf{S}\mathbf{U})y, \quad (\text{C2})$$

749 where $\mathbf{Q} = [Q_1, \dots, Q_{n_{\max}}]^T$, $\mathbf{U} = [U_1, \dots, U_{n_{\max}}]^T$, and $\mathbf{V} = [V_1, \dots, V_{n_{\max}}]^T$. Zonal and merid-
 750 ional background PV gradients, Q_x and Q_y , respectively, are

$$\begin{aligned} \mathbf{Q}_x &= \mathbf{S}\mathbf{V}, \\ \mathbf{Q}_y &= \beta - \mathbf{S}\mathbf{U}. \end{aligned} \quad (\text{C3})$$

751 Inserting a wave ansatz, $\psi_n = \text{Re} [\hat{\psi}_n e^{i(k_x x + k_y y - \omega t)}]$, into the linearized PV equation (C1), we get

$$i(k_x U_n + k_y V_n - \omega)\hat{q}_n + (ik_x Q_{ny} - ik_y Q_{nx})\hat{\psi}_n = 0, \quad (\text{C4})$$

752 where the relationship between $\hat{\mathbf{q}} = [\hat{q}_1, \dots, \hat{q}_{n_{\max}}]^T$ and $\hat{\boldsymbol{\psi}} = [\hat{\psi}_1, \dots, \hat{\psi}_{n_{\max}}]^T$ is given by equation
 753 (B3),

$$\hat{\mathbf{q}} = (\mathbf{S} - k^2 \mathbf{I}) \hat{\boldsymbol{\psi}}, \quad (\text{C5})$$

754 Equation (C4) forms a generalized eigenvalue problem for the mode $\hat{\boldsymbol{\psi}}$ (eigenvectors) and the
 755 frequency ω (eigenvalues),

$$\omega \mathbf{A} \hat{\boldsymbol{\psi}} = [(k_x \mathbf{U} + k_y \mathbf{V})\mathbf{A} + k_x \mathbf{Q}_y - k_y \mathbf{Q}_x] \hat{\boldsymbol{\psi}}, \quad (\text{C6})$$

756 where $\mathbf{A} = \mathbf{S} - k^2 \mathbf{I}$. For $\omega = \omega_r + i\sigma$, if the imaginary component, $\sigma > 0$, then the mode will grow
 757 exponentially, which signals a linear instability.

758 References

759 Adcroft, A., and Coauthors, 2019: The GFDL global ocean and sea ice model OM4.0: Model
 760 description and simulation features. *J. Adv. Model. Earth Sys.*, **11** (10), 3167–3211.

761 Aoki, K., A. Kubokawa, H. Sasaki, and Y. Sasai, 2009: Midlatitude baroclinic rossby waves in a
 762 high-resolution ogcm simulation. *J. Phys. Oceanogr.*, **39** (9), 2264–2279.

- 763 Blumen, W., 1978: Uniform potential vorticity flow: Part I. Theory of wave interactions and
764 two-dimensional turbulence. *Journal of the Atmospheric Sciences*, **35** (5), 774–783.
- 765 Bobrovich, A., and G. Reznik, 1999: Planetary waves in a stratified ocean of variable depth. part
766 2. continuously stratified ocean. *Journal of Fluid Mechanics*, **388**, 147–169.
- 767 Bretherton, F. P., 1966: Critical layer instability in baroclinic flows. *Quarterly Journal of the Royal*
768 *Meteorological Society*, **92** (393), 325–334.
- 769 Brink, K., and J. Pedlosky, 2020: The structure of baroclinic modes in the presence of baroclinic
770 mean flow. *Journal of Physical Oceanography*, **50** (1), 239–253.
- 771 Callies, J., G. Flierl, R. Ferrari, and B. Fox-Kemper, 2016: The role of mixed-layer instabilities in
772 submesoscale turbulence. *Journal of Fluid Mechanics*, **788**, 5–41.
- 773 Capet, X., J. C. McWilliams, M. J. Molemaker, and A. F. Shchepetkin, 2008: Mesoscale to
774 submesoscale transition in the California Current System. part III: Energy balance and flux. *J.*
775 *Phys. Oceanogr.*, **38** (10), 2256–2269.
- 776 Capet, X., G. Roulet, P. Klein, and G. Maze, 2016: Intensification of upper-ocean submesoscale
777 turbulence through Charney baroclinic instability. *J. Phys. Oceanogr.*, **46** (11), 3365–3384.
- 778 Chang, C.-Y., A. Adcroft, L. Zanna, R. W. Hallberg, and S. M. Griffies, 2023: Remote versus local
779 impacts of energy backscatter on the north atlantic sst biases in a global ocean model. *Submitted*
780 *to Geophysical Research Letters*.
- 781 Chang, C.-Y., and I. M. Held, 2019: The control of surface friction on the scales of baroclinic
782 eddies in a homogeneous quasigeostrophic two-layer model. *J. Atmos. Sci.*, **76** (6), 1627–1643.
- 783 Chang, C.-Y., and I. M. Held, 2021: The parameter dependence of eddy heat flux in a homoge-
784 neous Quasigeostrophic two-layer model on a β plane with quadratic friction. *Journal of the*
785 *Atmospheric Sciences*, **78** (1), 97–106.
- 786 Charney, J. G., 1947: The dynamics of long waves in a baroclinic westerly current. *Journal of the*
787 *Atmospheric Sciences*, **4** (5), 136–162.
- 788 Charney, J. G., 1971: Geostrophic turbulence. *J. Atmos. Sci.*, **28** (6), 1087–1095.

- 789 Danabasoglu, G., and J. Marshall, 2007: Effects of vertical variations of thickness diffusivity in an
790 ocean general circulation model. *Ocean Modelling*, **18** (2), 122–141.
- 791 de La Lama, M. S., J. LaCasce, and H. K. Fuhr, 2016: The vertical structure of ocean eddies.
792 *Dynamics and Statistics of the Climate System*, **1** (1).
- 793 Dong, J., B. Fox-Kemper, H. Zhang, and C. Dong, 2020: The seasonality of submesoscale energy
794 production, content, and cascade. *Geophysical Research Letters*, **47** (6), e2020GL087388.
- 795 Eady, E. T., 1949: Long waves and cyclone waves. *Tellus*, **1** (3), 33–52.
- 796 Eden, C., M. Jochum, and G. Danabasoglu, 2009: Effects of different closures for thickness
797 diffusivity. *Ocean Modelling*, **26** (1-2), 47–59.
- 798 Feng, L., C. Liu, A. Köhl, D. Stammer, and F. Wang, 2021: Four types of baroclinic instability
799 waves in the global oceans and the implications for the vertical structure of mesoscale eddies.
800 *Journal of Geophysical Research: Oceans*, **126** (3), e2020JC016966.
- 801 Feng, L., C. Liu, A. Köhl, and F. Wang, 2022: Seasonality of four types of baroclinic instability in
802 the global oceans. *Journal of Geophysical Research: Oceans*, **127** (5), e2022JC018572.
- 803 Ferrari, R., and C. Wunsch, 2009: Ocean circulation kinetic energy: Reservoirs, sources, and
804 sinks. *Annu. Rev. Fluid Mech.*, **41**, 253–282.
- 805 Fox-Kemper, B., R. Ferrari, and R. Hallberg, 2008a: Parameterization of mixed layer eddies. part
806 I: Theory and diagnosis. *J. Phys. Oceanogr.*, **38** (6), 1145–1165.
- 807 Fox-Kemper, B., R. Ferrari, and R. Hallberg, 2008b: Parameterization of mixed layer eddies. Part
808 I: Theory and diagnosis. *J. Phys. Oceanogr.*, **38** (6), 1145–1165.
- 809 Frenger, I., M. Münnich, N. Gruber, and R. Knutti, 2015: Southern Ocean eddy phenomenology.
810 *J. Geophys. Res. Oceans*, **120** (11), 7413–7449.
- 811 Fresnay, S., A. Ponte, S. Le Gentil, and J. Le Sommer, 2018: Reconstruction of the 3-D dynamics
812 from surface variables in a high-resolution simulation of North Atlantic. *Journal of Geophysical
813 Research: Oceans*, **123** (3), 1612–1630.
- 814 Fu, L.-L., and G. R. Flierl, 1980: Nonlinear energy and enstrophy transfers in a realistically
815 stratified ocean. *Dynamics of Atmospheres and Oceans*, **4** (4), 219–246.

- 816 Gallet, B., and R. Ferrari, 2020: The vortex gas scaling regime of baroclinic turbulence. *Proc.*
817 *Natl. Acad. Sci. USA*, **117** (9), 4491–4497.
- 818 Gallet, B., and R. Ferrari, 2021: A quantitative scaling theory for meridional heat transport in
819 planetary atmospheres and oceans. *AGU Advances*, **2** (3), e2020AV000 362.
- 820 Gill, A., 1982: *Atmosphere-Ocean Dynamics*, International Geophysics Series, Vol. 30. Academic
821 Press, London, 662 + xv pp.
- 822 Gnanadesikan, A., M.-A. Pradal, and R. Abernathey, 2015: Isopycnal mixing by mesoscale eddies
823 significantly impacts oceanic anthropogenic carbon uptake. *Geophys. Res. Lett.*, **42** (11), 4249–
824 4255.
- 825 González-Haro, C., and J. Isern-Fontanet, 2014: Global ocean current reconstruction from alti-
826 metric and microwave SST measurements. *Journal of Geophysical Research: Oceans*, **119** (6),
827 3378–3391.
- 828 Griffies, S. M., and R. W. Hallberg, 2000: Biharmonic friction with a smagorinsky-like viscosity for
829 use in large-scale eddy-permitting ocean models. *Monthly Weather Review*, **128** (8), 2935–2946.
- 830 Griffies, S. M., and Coauthors, 2015: Impacts on ocean heat from transient mesoscale eddies in a
831 hierarchy of climate models. *Journal of Climate*, **28** (3), 952–977.
- 832 Groeskamp, S., J. H. LaCasce, T. J. McDougall, and M. Rogé, 2020: Full-depth global esti-
833 mates of ocean mesoscale eddy mixing from observations and theory. *Geophys. Res. Lett.*,
834 e2020GL089425.
- 835 Hallberg, R., 1997: Localized coupling between surface and bottom-intensified flow over topog-
836 raphy. *J. Phys. Oceanogr.*, **27** (6), 977–998.
- 837 Hausmann, U., and A. Czaja, 2012: The observed signature of mesoscale eddies in sea surface
838 temperature and the associated heat transport. *Deep Sea Res. I*, **70**, 60–72.
- 839 Held, I. M., and V. D. Larichev, 1996: A scaling theory for horizontally homogeneous, baroclini-
840 cally unstable flow on a beta plane. *J. Atmos. Sci.*, **53** (7), 946–952.
- 841 Held, I. M., R. T. Pierrehumbert, S. T. Garner, and K. L. Swanson, 1995: Surface quasi-geostrophic
842 dynamics. *Journal of Fluid Mechanics*, **282**, 1–20.

- 843 Holland, W. R., and P. B. Rhines, 1980: An example of eddy-induced ocean circulation. *J. Phys.*
844 *Oceanogr.*, **10** (7), 1010–1031.
- 845 Holmes, R. M., S. Groeskamp, K. D. Stewart, and T. J. McDougall, 2022: Sensitivity of a coarse-
846 resolution global ocean model to a spatially variable neutral diffusivity. *Journal of Advances in*
847 *Modeling Earth Systems*, **14** (3), e2021MS002 914.
- 848 Isern-Fontanet, J., G. Lapeyre, P. Klein, B. Chapron, and M. W. Hecht, 2008: Three-dimensional
849 reconstruction of oceanic mesoscale currents from surface information. *Journal of Geophysical*
850 *Research: Oceans*, **113** (C9).
- 851 Isern-Fontanet, J., M. Shinde, and C. González-Haro, 2014: On the transfer function between
852 surface fields and the geostrophic stream function in the Mediterranean Sea. *J. Phys. Oceanogr.*,
853 **44** (5), 1406–1423.
- 854 Jansen, M. F., A. Adcroft, S. Khani, and H. Kong, 2019: Toward an energetically consistent,
855 resolution aware parameterization of ocean mesoscale eddies. *J. Adv. Model. Earth Sys.*, **11** (8),
856 2844–2860.
- 857 Jansen, M. F., A. J. Adcroft, R. Hallberg, and I. M. Held, 2015: Parameterization of eddy fluxes
858 based on a mesoscale energy budget. *Ocean Modell.*, **92**, 28–41.
- 859 Juricke, S., S. Danilov, N. Koldunov, M. Oliver, and D. Sidorenko, 2020: Ocean kinetic energy
860 backscatter parametrization on unstructured grids: Impact on global eddy-permitting simula-
861 tions. *Journal of Advances in Modeling Earth Systems*, **12** (1), e2019MS001 855.
- 862 Juricke, S., S. Danilov, A. Kutsenko, and M. Oliver, 2019: Ocean kinetic energy backscatter
863 parametrizations on unstructured grids: Impact on mesoscale turbulence in a channel. *Ocean*
864 *Modelling*, **138**, 51–67.
- 865 Khatri, H., S. M. Griffies, T. Uchida, H. Wang, and D. Menemenlis, 2021: Role of Mixed-Layer
866 Instabilities in the Seasonal Evolution of Eddy Kinetic Energy Spectra in a Global Submesoscale
867 Permitting Simulation. *Geophysical Research Letters*, **48** (18), 1–13, <https://doi.org/10.1029/2021GL094777>.
- 868
869 Killworth, P. D., 1992: An equivalent-barotropic mode in the fine resolution antarctic model.
870 *Journal of Physical Oceanography*, **22** (11), 1379–1387.

- 871 Klein, P., J. Isern-Fontanet, G. Lapeyre, G. Roullet, E. Danioux, B. Chapron, S. Le Gentil, and
872 H. Sasaki, 2009: Diagnosis of vertical velocities in the upper ocean from high resolution sea
873 surface height. *Geophys. Res. Lett.*, **36** (12).
- 874 Klocker, A., and R. Abernathy, 2014: Global patterns of mesoscale eddy properties and diffusiv-
875 ities. *J. Phys. Oceanogr.*, **44** (3), 1030–1046.
- 876 Kong, H., and M. Jansen, 2017: The eddy diffusivity in barotropic β -plane turbulence. *Fluids*,
877 **2** (4), 54.
- 878 Lacasce, J. H., 2017: The prevalence of oceanic surface modes. *Geophys. Res. Lett.*, **44** (21),
879 11–097.
- 880 LaCasce, J. H., and A. Mahadevan, 2006: Estimating subsurface horizontal and vertical velocities
881 from sea-surface temperature. *J. Mar. Res.*, **64** (5), 695–721.
- 882 Lapeyre, G., 2009: What vertical mode does the altimeter reflect? On the decomposition in
883 baroclinic modes and on a surface-trapped mode. *J. Phys. Oceanogr.*, **39** (11), 2857–2874.
- 884 Lapeyre, G., 2017: Surface quasi-geostrophy. *Fluids*, **2** (1), 7.
- 885 Lapeyre, G., and P. Klein, 2006: Dynamics of the upper oceanic layers in terms of surface
886 quasigeostrophy theory. *J. Phys. Oceanogr.*, **36** (2), 165–176.
- 887 Larichev, V. D., and I. M. Held, 1995: Eddy amplitudes and fluxes in a homogeneous model of
888 fully developed baroclinic instability. *J. Phys. Oceanogr.*, **25** (10), 2285–2297.
- 889 Liu, L., S. Peng, and R. X. Huang, 2017: Reconstruction of ocean’s interior from observed sea
890 surface information. *Journal of Geophysical Research: Oceans*, **122** (2), 1042–1056.
- 891 Liu, L., S. Peng, J. Wang, and R. X. Huang, 2014: Retrieving density and velocity fields of
892 the ocean’s interior from surface data. *Journal of Geophysical Research: Oceans*, **119** (12),
893 8512–8529.
- 894 Loose, N., G. M. Marques, A. Adcroft, S. D. Bachman, S. M. Griffies, I. Grooms, R. W. Hallberg,
895 and M. F. Jansen, 2022: Parameterizing eddy form stress in a thickness-weighted average
896 isopycnal ocean model.

- 897 Marques, G., and Coauthors, 2022: Neverworld2: An idealized model hierarchy to investigate
898 ocean mesoscale eddies across resolutions. *EGUsphere*, 1–20.
- 899 Marshall, J., and K. Speer, 2012: Closure of the meridional overturning circulation through
900 Southern Ocean upwelling. *Nature Geosci.*, **5** (3), 171.
- 901 Miracca-Lage, M., C. González-Haro, D. C. Napolitano, J. Isern-Fontanet, and P. S. Polito, 2022:
902 Can the surface quasi-geostrophic (SQG) theory explain upper ocean dynamics in the South
903 Atlantic? *Journal of Geophysical Research: Oceans*, **127** (2), e2021JC018 001.
- 904 Ni, Q., X. Zhai, J. LaCasce, D. Chen, and D. Marshall, 2023: Full-depth eddy kinetic energy in
905 the global ocean estimated from altimeter and argo observations. *Geophysical Research Letters*.
- 906 Phillips, N. A., 1954: Energy transformations and meridional circulations associated with simple
907 baroclinic waves in a two-level, quasi-geostrophic model. *Tellus*, **6** (3), 274–286.
- 908 Pierrehumbert, R., and K. Swanson, 1995: Baroclinic instability. *Annual review of fluid mechanics*,
909 **27** (1), 419–467.
- 910 Ponte, A. L., and P. Klein, 2013: Reconstruction of the upper ocean 3D dynamics from high-
911 resolution sea surface height. *Ocean Dynamics*, **63** (7), 777–791.
- 912 Qiu, B., S. Chen, P. Klein, H. Torres, J. Wang, L.-L. Fu, and D. Menemenlis, 2020: Reconstructing
913 upper-ocean vertical velocity field from sea surface height in the presence of unbalanced motion.
914 *Journal of Physical Oceanography*, **50** (1), 55–79.
- 915 Qiu, B., S. Chen, P. Klein, C. Ubelmann, L.-L. Fu, and H. Sasaki, 2016: Reconstructability of
916 three-dimensional upper-ocean circulation from SWOT sea surface height measurements. *J.*
917 *Phys. Oceanogr.*, **46** (3), 947–963.
- 918 Quan, Q., and Coauthors, 2023: Observed oceanic surface modes in the northern south china sea.
919 *Journal of Physical Oceanography*.
- 920 Radko, T., 2023: A generalized theory of flow forcing by rough topography. *Journal of Fluid*
921 *Mechanics*, **961**, A24.
- 922 Rhines, P., 1970: Edge-, bottom-, and Rossby waves in a rotating stratified fluid. *Geophys.*
923 *Astrophys. Fluid Dyn.*, **1** (3-4), 273–302.

- 924 Rhines, P. B., 1975: Waves and turbulence on a beta-plane. *J. Fluid Mech.*, **69** (3), 417–443.
- 925 Rhines, P. B., and W. R. Young, 1982: Homogenization of potential vorticity in planetary gyres.
926 *Journal of Fluid Mechanics*, **122**, 347–367.
- 927 Roulet, G., J. C. McWilliams, X. Capet, and M. J. Molesmaker, 2012: Properties of steady
928 geostrophic turbulence with isopycnal outcropping. *J. Phys. Oceanogr.*, **42** (1), 18–38.
- 929 Salmon, R., 1980: Baroclinic instability and geostrophic turbulence. *Geophysical & Astrophysical*
930 *Fluid Dynamics*, **15** (1), 167–211.
- 931 Samelson, R., 1992: Surface-intensified Rossby waves over rough topography. *J. Mar. Res.*, **50** (3),
932 367–384.
- 933 Sasaki, H., P. Klein, B. Qiu, and Y. Sasai, 2014: Impact of oceanic-scale interactions on the
934 seasonal modulation of ocean dynamics by the atmosphere. *Nature communications*, **5** (1), 1–8.
- 935 Schubert, R., J. Gula, R. J. Greatbatch, B. Baschek, and A. Biastoch, 2020: The submesoscale
936 kinetic energy cascade: Mesoscale absorption of submesoscale mixed layer eddies and frontal
937 downscale fluxes. *J. Phys. Oceanogr.*, **50** (9), 2573–2589.
- 938 Scott, R. B., and B. K. Arbic, 2007: Spectral energy fluxes in geostrophic turbulence: Implications
939 for ocean energetics. *J. Phys. Oceanogr.*, **37** (3), 673–688.
- 940 Smith, K. S., 2007: Eddy amplitudes in baroclinic turbulence driven by nonzonal mean flow: Shear
941 dispersion of potential vorticity. *J. Phys. Oceanogr.*, **37** (4), 1037–1050.
- 942 Smith, K. S., and G. K. Vallis, 2001: The scales and equilibration of midocean eddies: Freely
943 evolving flow. *Journal of Physical Oceanography*, **31** (2), 554–571.
- 944 Smith, K. S., and J. Vanneste, 2013: A surface-aware projection basis for quasigeostrophic flow. *J.*
945 *Phys. Oceanogr.*, **43** (3), 548–562.
- 946 Stanley, Z., S. Bachman, and I. Grooms, 2020: Vertical structure of ocean mesoscale eddies with im-
947 plications for parameterizations of tracer transport. *J. Adv. Model. Earth Sys.*, e2020MS002151.
- 948 Stone, P. H., 1972: A simplified radiative-dynamical model for the static stability of rotating
949 atmospheres. *J. Atmos. Sci.*, **29** (3), 405–418.

950 Storer, B. A., M. Buzzicotti, H. Khatri, S. M. Griffies, and H. Aluie, 2022: Global energy
951 spectrum of the general oceanic circulation. *Nature Communication*, **13**, [https://doi.org/10.](https://doi.org/10.1038/s41467-022-33031-3)
952 [1038/s41467-022-33031-3](https://doi.org/10.1038/s41467-022-33031-3).

953 Tailleux, R., and J. C. McWilliams, 2001: The effect of bottom pressure decoupling on the speed
954 of extratropical, baroclinic Rossby waves. *J. Phys. Oceanogr.*, **31** (6), 1461–1476.

955 Thompson, A. F., and W. R. Young, 2006: Scaling baroclinic eddy fluxes: Vortices and energy
956 balance. *J. Phys. Oceanogr.*, **36** (4), 720–738.

957 Tulloch, R., J. Marshall, C. Hill, and K. S. Smith, 2011: Scales, growth rates, and spectral fluxes
958 of baroclinic instability in the ocean. *J. Phys. Oceanogr.*, **41** (6), 1057–1076.

959 Vallis, G. K., 2017: *Atmospheric and oceanic fluid dynamics*. Cambridge University Press.

960 Visbeck, M., J. Marshall, T. Haine, and M. Spall, 1997: Specification of eddy transfer coefficients
961 in coarse-resolution ocean circulation models. *J. Phys. Oceanogr.*, **27** (3), 381–402.

962 Wang, J., G. R. Flierl, J. H. LaCasce, J. L. McClean, and A. Mahadevan, 2013: Reconstructing the
963 ocean’s interior from surface data. *J. Phys. Oceanogr.*, **43** (8), 1611–1626.

964 Wolfe, C. L., and P. Cessi, 2010: What sets the strength of the middepth stratification and
965 overturning circulation in eddying ocean models? *J. Phys. Oceanogr.*, **40** (7), 1520–1538.

966 Wortham, C., and C. Wunsch, 2014: A multidimensional spectral description of ocean variability.
967 *J. Phys. Oceanogr.*, **44** (3), 944–966.

968 Wunsch, C., 1997: The vertical partition of oceanic horizontal kinetic energy. *J. Phys. Oceanogr.*,
969 **27** (8), 1770–1794.

970 Yankovsky, E., S. Bachman, K. S. Smith, and L. Zanna, 2023: Backscatter parameterization of
971 ocean mesoscale eddies informed by vertical structure. *Submitted to Journal of Advances in*
972 *Modeling Earth Systems*.

973 Yankovsky, E., L. Zanna, and K. S. Smith, 2022: Influences of mesoscale ocean eddies on flow
974 vertical structure in a resolution-based model hierarchy. *Journal of Advances in Modeling Earth*
975 *Systems*, e2022MS003203.

- 976 Yassin, H., and S. M. Griffies, 2022a: On the discrete normal modes of quasigeostrophic theory.
977 *Journal of Physical Oceanography*, **52** (2), 243–259.
- 978 Yassin, H., and S. M. Griffies, 2022b: Surface quasigeostrophic turbulence in variable stratification.
979 *Journal of Physical Oceanography*, **52** (12), 2995–3013.
- 980 Zhang, W., and C. L. Wolfe, 2022: On the vertical structure of oceanic mesoscale tracer diffusivities.
981 *Journal of Advances in Modeling Earth Systems*, **14** (6), e2021MS002 891.
- 982 Zhang, X., Z. Jing, and P. Yang, 2023: Seasonality of upper-ocean vertical eddy buoyancy flux in
983 the kuroshio extension. *Journal of Physical Oceanography*.
- 984 Zhang, Z., Y. Zhang, and W. Wang, 2017: Three-compartment structure of subsurface-intensified
985 mesoscale eddies in the ocean. *J. Geophys. Res. Oceans*, **122** (3), 1653–1664.
- 986 Zhang, Z., Y. Zhang, W. Wang, and R. Huang, 2013: Universal structure of mesoscale eddies in
987 the ocean. *Geophys. Res. Lett.*, **40**, 3677–3681.